JCB Journal of Cell Biology

ARTICLE

Proteins that control the geometry of microtubules at the ends of cilia

Panagiota Louka[1], Krishna Kumar Vasudevan[1], Mayukh Guha[1], Ewa Joachimiak[2], Dorota Wloga[2], Raphaël F.-X. Tomasi[3], Charles N. Baroud[3], Pascale Dupuis-Williams[4,5], Domenico F. Galati[6], Chad G. Pearson[6], Luke M. Rice[7], James J. Moresco[8], John R. Yates III[8], Yu-Yang Jiang[1], Karl Lechtreck[1], William Dentler[9], and Jacek Gaertig[1]

Cilia, essential motile and sensory organelles, have several compartments: the basal body, transition zone, and the middle and distal axoneme segments. The distal segment accommodates key functions, including cilium assembly and sensory activities. While the middle segment contains doublet microtubules (incomplete B-tubules fused to complete A-tubules), the distal segment contains only A-tubule extensions, and its existence requires coordination of microtubule length at the nanometer scale. We show that three conserved proteins, two of which are mutated in the ciliopathy Joubert syndrome, determine the geometry of the distal segment, by controlling the positions of specific microtubule ends. FAP256/CEP104 promotes A-tubule elongation. CHE-12/Crescerin and ARMC9 act as positive and negative regulators of B-tubule length, respectively. We show that defects in the distal segment dimensions are associated with motile and sensory deficiencies of cilia. Our observations suggest that abnormalities in distal segment organization cause a subset of Joubert syndrome cases.

Introduction

Microtubules function in groups, such as networks and bundles, within which the positions and dimensions of individual filaments have to be precisely coordinated in space and time. Cilia are conserved organelles that are built around a sophisticated bundle of microtubules, the axoneme. With few exceptions, motile cilia have a 9+2 axoneme containing nine outer and two central pair (CP) microtubules, while most sensory cilia have a 9+0 axoneme that lacks the CP. The ring of nine outer microtubules is the unifying feature of both motile and sensory cilia. For most of their length, the outer microtubules have a doublet conformation and are composed of a "complete" A-tubule and an "incomplete" B-tubule that is fused to the A-tubule wall. Importantly, in almost all known cilia, the B-tubules are shorter than the A-tubules; this difference in length creates the distal ciliary segment made only of singlet microtubules (Fig. 1 A; Satir, 1968).

The distal segment is the site of axoneme assembly, and a preexisting A-tubule may function as a template for the B-tubule assembly (Ichikawa et al., 2017). In addition, the distal segment may play a role in signaling because it tends to be relatively long in sensory cilia. In the olfactory cilia that are particularly long (Reese, 1965; Moran et al., 1982), the distal segment represents 80% of total cilium length and this compartment is enriched in signaling proteins that mediate olfaction (McEwen et al., 2008). Important signaling proteins, including the Hedgehog (Hh) pathway components, Gli and Sufu and the G protein–coupled receptor SSTR3, accumulate in the distal segment of the primary cilium in activated cells (Haycraft et al., 2005; Ye et al., 2018).

While the distal segment is a feature of almost all cilia, the mechanism of its biogenesis is not clear. In *Caenorhabditis elegans*, mutations in either axonemal tubulin or in the intraflagellar transport (IFT) proteins, OSM-3 and DYF-1, shorten the distal segment in the cilia of the amphid channel neurons (Perkins et al., 1986; Snow et al., 2004; Ou et al., 2005; Evans et al., 2006; Mukhopadhyay et al., 2007; Hao et al., 2011). The contribution of OSM-3 to the distal segment biogenesis is particularly well studied. OSM-3 forms a homodimeric kinesin-2 motor that functions in the anterograde IFT (Signor et al., 1999) along with the heterotrimeric kinesin-2, kinesin-II (Cole et al., 1993). In the amphid channel cilia, these two motors cooperate to build the middle segment, but only OSM-3 enters the distal segment, and its loss

[1]Department of Cellular Biology, University of Georgia, Athens, GA; [2]Laboratory of Cytoskeleton and Cilia Biology, Nencki Institute of Experimental Biology of Polish Academy of Sciences, Warsaw, Poland; [3]Department of Mechanics, LadHyX, Ecole Polytechnique-Centre National de la Recherche Scientifique, Palaiseau, France; [4]UMR-S1174 Institut National de la Santé et de la Recherche Médicale, Université Paris-Sud, Bat 443, Orsay, France; [5]École Supérieure de Physique et de Chimie Industrielles de la Ville de Paris, Paris, France; [6]Department of Cell and Developmental Biology, University of Colorado Anschutz Medical Campus, Aurora, CO; [7]Departments of Biophysics and Biochemistry, University of Texas Southwestern Medical Center, Dallas, TX; [8]Department of Molecular Medicine, The Scripps Research Institute, La Jolla, CA; [9]Department of Molecular Biosciences, University of Kansas, Lawrence, KS.

Correspondence to Jacek Gaertig: jgaertig@uga.edu; William Dentler: wdent@ku.edu.

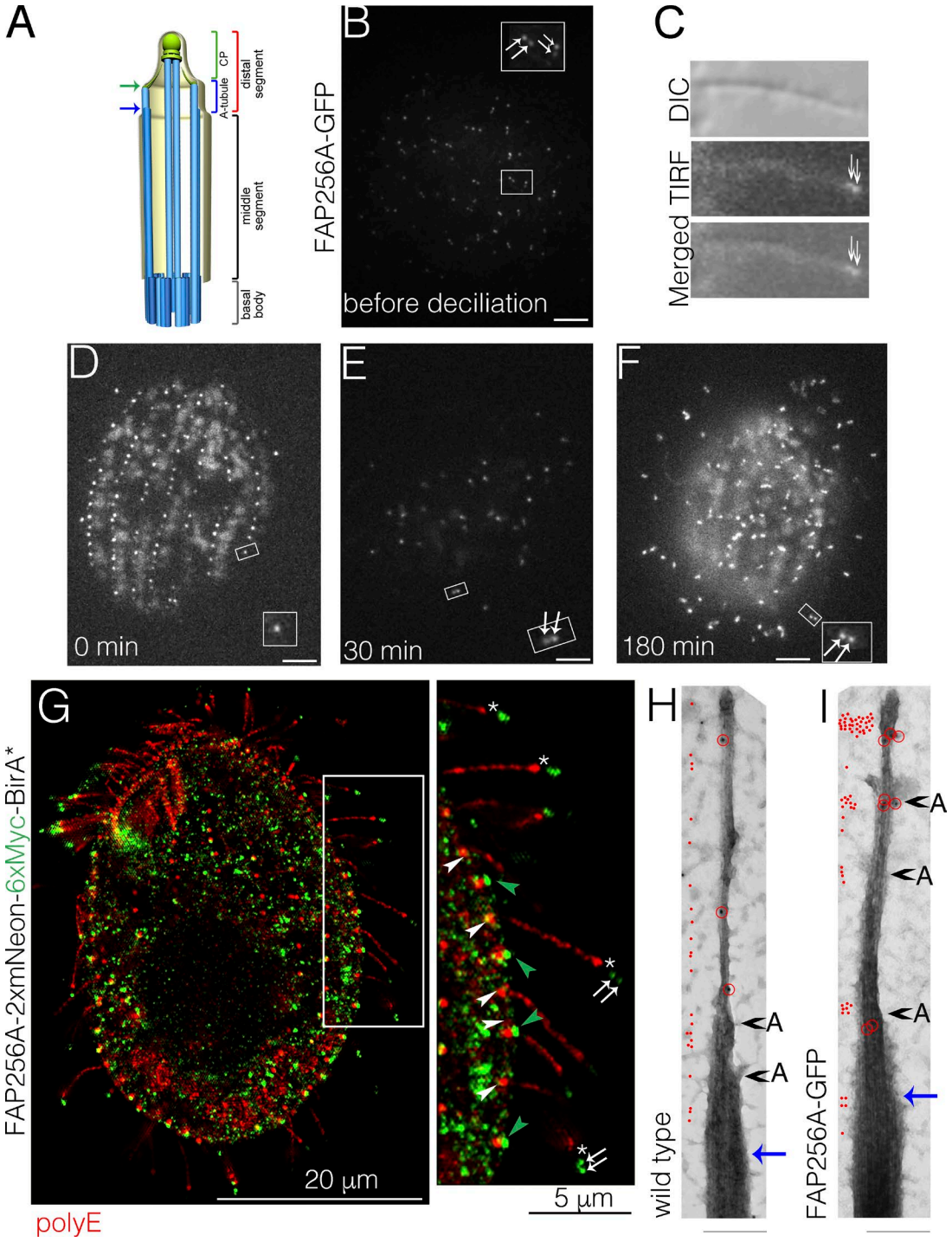

Figure 1. **FAP256A localizes to the tips of cilia and unciliated basal bodies and the ends of A-tubules and CP. (A)** The segmental organization of the motile cilium (the blue and green arrows mark the proximal boundary of the distal segment and the CP region, respectively). **(B and D–F)** TIRFM imaging of live *Tetrahymena* cells that express FAP256A-GFP under native promoter at several times before and after low pH–induced deciliation (bar, 5 µm). **(C)** Differential interference contrast (DIC) and TIRFM images of the same cilium (white arrows, FAP256A-GFP dots at the tip). **(G)** An SR-SIM immunofluorescence image of a *Tetrahymena* cell expressing FAP256A-2xmNeonGreen-6xMyc-BirA* under native promoter (green, 6xMyc; red, polyE; green arrowheads, unciliated basal bodies; white arrowheads, ciliated basal bodies; white arrows, FAP256A signals at the tip; asterisks mark the gap between the polyE tubulin and FAP256A signals). **(H and I)** Immunoelectron TEM localization of FAP256A-GFP. Axonemes of wild type (H) and FAP256A-GFP (I) cells were labeled with anti-GFP and gold-conjugated secondary antibodies. Red circles mark the gold particles on the axonemes. The red dots on the left side summarize the approximate positions of gold particles (one red dot denotes one gold particle) found in a total of 14 wild-type and 14 FAP256A-GFP axonemes. The As mark the visible termination points for the A-tubules (note that less than nine ends are visible, some of the ends could be on the nonimaged side of the axoneme or were lost during preparation), and the blue arrows mark the proximal boundary of the distal segment (bar, 200 nm).

leads to a severe shortening of the distal segment (Snow et al., 2004; Evans et al., 2006; Mukhopadhyay et al., 2007; Prevo et al., 2015). However, OSM-3 is not needed for the distal segment assembly in the AWB amphid cilia (Mukhopadhyay et al., 2007). An OSM-3 orthologue, KIF17, is targeted to the tip of primary cilia in mammalian cells and interacts with KIF7 (Schwarz et al., 2017), a kinesin-4 that destabilizes the ends of axonemal microtubules (He et al., 2014). KIF17 itself stabilizes the cytoplasmic microtubules in mammalian epithelial cells (Jaulin and Kreitzer, 2010), but it is not clear whether OSM-3/KIF17 homologues affect the dynamics of ciliary microtubules. The vertebrate orthologues of OSM-3/KIF17 are not needed for the biogenesis of the outer segment of photoreceptor cells in the mouse and zebrafish (Jiang et al., 2015a; Lewis et al., 2017). The outer segments of vertebrate photoreceptors contain axonemes with microtubule doublets that transit into singlet extensions (Roof et al., 1991; Insinna et al., 2008). Thus, in the vertebrate photoreceptors either OSM-3/KIF17 is not required for the formation of singlet extensions, or the presence of a distal ciliary segment is not required for the differentiation of photoreceptors. Overall, both the functional significance and the biogenesis of the distal segment remain unclear. Furthermore, the mechanisms that individualize the lengths of microtubules across the axoneme and establish its functional compartments, including the distal segment, have not emerged yet.

Here, we use the multiciliated protist *Tetrahymena* to explore the biogenesis and function of the ciliary distal segment. We found that three conserved ciliary proteins, FAP256/CEP104, CHE-12/Crescerin, and ARMC9, localize near the boundaries of the distal segment where they control the positions of the ends of specific types of axonemal microtubules, and consequently contribute to the geometry of the distal segment. Since mutations in two proteins studied here (ARMC9 and FAP256/CEP104) cause Joubert syndrome, our observations suggest that abnormalities in the distal segment cause a subset of this ciliopathy, possibly by interfering with signaling molecules that operate near the ciliary tip.

Results

FAP256/CEP104, CHE-12/Crescerin, and ARMC9 are enriched near the boundaries of the distal segment

In *Chlamydomonas reinhardtii*, FAP256/CEP104 protein is enriched near the ends of ciliary microtubules, and its loss alters the shape of the ciliary tip and reduces ciliogenesis (Satish Tammana et al., 2013). FAP256/CEP104 has a TOG domain (Jiang et al., 2012; Rezabkova et al., 2016; Al-Jassar et al., 2017). Most TOG domains bind to tubulin in a "curved conformation" that is characteristic of the unpolymerized state and also transiently present at the growing microtubule plus end (Ayaz et al., 2012, 2014). *Tetrahymena thermophila* has two genes that encode FAP256/CEP104 homologues: *TTHERM_00079820* (*FAP256A*) and *TTHERM_00584800* (*FAP256B*). The most compatible structure to the sequences of the predicted TOG-domains of FAP256A and FAP256B is TOG1 of yeast STU2 (based on the i-TASSER searches with no template specificity). A threading of the amino acid sequences of the TOG domains of FAP256A and FAP256B on the 3D structure of TOG1 of STU2 revealed conservation of key amino acids at the interphases with curved tubulin (Fig. S1, A–C; data not shown for FAP256B). Thus, FAP256A and FAP256B have TOG domains that are compatible with the plus ends of microtubules such as those present near the tips of cilia. Indeed, FAP256A-GFP was enriched near the tips of steady-state cilia (arrows, Fig. 1 B, C, and G; and Video 1), assembling cilia (Fig. 1, D–F), and unciliated basal bodies (green arrowheads, Fig. 1 G). At the tips of most cilia of either live (using total internal reflection microscopy [TIRFM]) or fixed (using super-resolution structured illumination [SR-SIM]) cells, there were two dots of tagged FAP256A (Fig. 1, B, C, and G; in Video 1, note that pairs of dots move together). We used immunogold transmission electron microscopy (TEM) to localize FAP256A-GFP with higher resolution. At the ultrastructural level, the distal segment of a 9+2 cilium can be divided into two subcompartments: (1) the "A-tubule region" that contains the A-tubule (singlet) extensions and a portion of the CP and (2) the more distal "CP region" that contains only the central microtubules (Fig. 1 A; Sale and Satir, 1976; Dentler, 1980). On the electron micrographs of whole-mounted cilia or axonemes that are inspected from the base toward the tip, the cilium width decreases near the area containing the termination points of the B-tubules (Fig. S2 M; Reynolds et al., 2018); within this transitional region, the stain intensity of the axoneme in whole-mounted cilia decreases, likely due to the termination of the radial spokes and dynein arms (red line in Fig. 5 E). Consistently, on the cross sections that span the transitional region, the singlets (but not the doublets on the same cross sections) lacked radial spokes. Furthermore, the singlets (and the associated portions of the plasma membrane) were positioned closer to the axoneme center as compared with the doublet microtubules (Fig. S5, I–K). Thus, the level at which the cilium tapers off could be used as the approximate proximal boundary of the distal segment (blue arrow, Fig. 1 A, H, and I). The proximal boundary of the CP region was designated at the level where the axoneme becomes maximally thin (green arrow, Fig. 1 A and Fig. 5 E; and Fig. S2 M). The A-tubule region is located between these two landmarks (blue brackets, Fig. 1 A and Fig. 5 E).

In cilia of cells expressing FAP256A-GFP, analyzed by immunogold TEM, there was a strong enrichment of gold particles near the end of the CP and a weaker (but above background) signal scattered along the A-tubule region (Fig. 1, H and I). We used a complementary approach, based on tubulin post-translational modifications (PTMs), to localize FAP256A-GFP. PolyG and polyE antibodies recognize PTMs that are enriched on the B-tubules (Lechtreck and Geimer, 2000; Kubo et al., 2010; Suryavanshi et al., 2010). Immunogold TEM confirmed that the specific polyG signal ends near the B-tubule termination zone (Fig. S2, A and B). In SR-SIM, there is a gap of 840 ± 200 nm (n = 30 cilia) between the proximal FAP256A-6xMyc dot and the distal end of either polyG (asterisks, Fig. S3 A) or polyE (asterisks, Fig. 1 G) signals. Based on the measurements of the distal segment dimensions in whole-mounted wild-type cilia (Fig. 5 E and Fig. S2 L), the proximal dot of FAP256A-6xmyc is located within the A-tubule region. Using the average length of the A-tubule region and the frequencies of TEM cross sections with different numbers of A-tubule profiles (Fig. S2, C–K), we estimated that the termination points

of the individual A-tubules spread over ∼540 nm (Fig. S2 L; this is close to the published observations in isolated axonemes [Sale and Satir, 1976]). Among the nine A-tubule ends, six of them terminate within ∼100 nm from each other, which is close to the resolution limit of SR-SIM. While the positions of the three remaining A-tubule ends are far enough from others to be resolved in principle, in practice the signal intensity of tagged FAP256A associated with a single microtubule end is likely below the sensitivity of SR-SIM. Thus, the proximal FAP256A-GFP dot seen in SR-SIM likely represents a cluster of A-tubule ends. The two FAP256A-GFP dots (in SR-SIM) are separated by 590 ± 90 nm (n = 30 cilia), which corresponds to the length of the CP region (582 ± 234 nm, Fig. 5, E and L; and Fig. S2 L). Taking together the SR-SIM and TEM imaging, FAP256A-GFP likely colocalizes with the ends of complete microtubules: CP and A-tubules. We did not detect the tagged FAP256B even after its overexpression.

CHE-12/Crescerin is the only other known ciliary TOG domain protein, whose loss shortens the amphid cilia in *C. elegans* (Perkins et al., 1986; Bacaj et al., 2008; Das et al., 2015). *Tetrahymena* has two genes encoding CHE-12/Crescerin: *TTHERM_00102840* (*CHE12A*) and *TTHERM_00193480* (*CHE12B*). In growing cells, CHE12A-GFP was enriched near the tips of shorter, assembling cilia and very close to the end of polyG, the marker of B-tubule ends (arrow, Fig. 2 A). Consistently, in cells regenerating cilia after deciliation, most ciliary tips were positive for CHE12A-GFP (Fig. 2 B). CHE12B-6xMyc was detected near the tips of full-length cilia, also very close to the end of either polyG or polyE signals (Fig. 2 C and Fig. S3 B). There were also weak puncta of CHE12B along the length of mature cilia (arrowheads, Fig. 2 C and Fig. S3 B), and TIRFM revealed that a subset of CHE12B-mNeonGreen particles diffused along the cilium length (Fig. 2, D and E; and Video 2). The enrichment close to the ends of polyG and polyE signals and the presence of TOG domains is consistent with localization of CHE12 near the ends of B-tubules.

We considered ARMC9A (TTHERM_00723450) as a potential distal segment-associated protein, based on (1) its proximity to an overproduced NRK2 kinase, a known distal segment marker (Wloga et al., 2006), which was revealed by BioID (Table S2), and (2) the similarity of its mRNA expression pattern to that of FAP256A (Xiong et al., 2013; Tsypin and Turkewitz, 2017). ARMC9A and its paralogue ARMC9B (TTHERM_00420850) are orthologues of the mammalian ARMC9, whose mutations cause Joubert syndrome (Van De Weghe et al., 2017; Kar et al., 2018). In most cilia, SR-SIM revealed an enrichment of ARMC9A-6xMyc very close to the end of polyG (Fig. 3 A). In isolated cilia with partially splayed axonemes, there were multiple foci of ARMC9A-6xMyc corresponding to the ends of splayed microtubules (Fig. 3 B). Immunogold TEM detection of ARMC9A-6xMyc revealed an enrichment of gold particles near the B-tubule termination zone (Fig. 3, C and D). ARMC9B-6xMyc localized to the unciliated basal bodies (arrowhead, Fig. 3 E) and the tips of growing cilia (Fig. 3 E, arrow shows the assembling oral cilia). In SR-SIM, the GFP-FAP256A and ARMC9A-mNeon-6xMyc signals were separated by ∼700 nm, consistent with their localizations to different compartments near the ends of cilia (Fig. 3 F). To conclude, we identified ARMC9 as a new distal segment boundary protein that, like CHE12, localizes near the ends of B-tubules.

FAP256, CHE12, and ARMC9 are important for cilia-based functions

To study the functions of FAP256, CHE12, and ARMC9, we created gene disruption strains (both paralogues were targeted for each of the three proteins). *Tetrahymena* cells use cilia for swimming, feeding by phagocytosis, and pair formation at the onset of conjugation. All three knockout (KO) strains swam slowly; the cells lacking ARMC9 (ARMC9-KO) were most affected and swam at the rate of 50% of the wild type (Fig. 4 A and Videos 3–6). The loss of ARMC9 also greatly reduced the rates of cell multiplication and phagocytosis (Fig. 4 B and Fig. S4 E). In ciliates, phagocytosis occurs at the bottom of the oral apparatus and requires motility of oral cilia. In the MEPP culture medium that bypasses the requirement for phagocytosis (Orias and Rasmussen, 1976), the ARMC9-KO cells grew almost as well as the wild type (Fig. S4, E and F). Thus, the slow multiplication of ARMC9-KO is largely due to its reduced feeding rate. Introduction of GFP-ARMC9B transgene into ARMC9-KO cells partially rescued the phagocytosis defect (Fig. 4 B).

The FAP256-KO and CHE12-KO cells had ∼30% fewer cilia, while the ARMC9-KO cells had 37% more cilia than the wild type, respectively (Fig. S4, A–D and G). It is thus possible that FAP256 and CHE12 contribute to (but are not required to) the ciliation of basal bodies. Because wild-type cells assemble more cilia in starvation (cilia density under growing conditions: 0.27 cilia/µm, ±0.05 n = 10 cells; starvation: 0.37 cilia/µm, ±0.04 n = 6 cells; Nelsen, 1978; Nelsen and Debault, 1978), the increased ciliation of ARMC9-KO cells could be a response to starvation caused by their slow phagocytosis. The length of cilia was normal in the FAP256-KO, reduced (by 16%) in CHE12-KO and increased (by 14%) in ARMC9-KO cells (Fig. 5 K). The ciliary beat frequency was reduced (by 15%) in FAP256-KO and unaffected in CHE12-KO cells (Fig. 4 D). The ciliary waveform appeared unaffected in the FAP256-KO and CHE12-KO cells (Videos 4 and 5). The ARMC9-KO cells showed the most severe defects in ciliary motility; many cilia (particularly those in the posterior cell region) were paralyzed or appeared to have incomplete power strokes (Fig. 4, E and F; and Video 6). The nonparalyzed ARMC9-KO cilia beat at the frequency of 43% of the wild type (Fig. 4 D).

Starved and sexually mature *Tetrahymena* cells form pairs at the onset of conjugation. FAP256-KO cells almost completely failed to form pairs with wild-type cells of a complementary mating type and this defect was partially rescued by the GFP-FAP256A transgene (Fig. 4 C). Cilia-less mutants do not form pairs (data not shown). The FAP256-KO cells have fewer cilia that beat slowly. However, other mutants that have even fewer cilia (CHE12-KO) or swim more slowly (ARMC9-KO) formed pairs more efficiently (Fig. 4 C). Thus, the pair formation defect in the FAP256-KO cells does not appear to be a downstream effect of weak ciliary motility, but rather may reflect a deficiency in the cell-to-cell signaling that occurs during pair formation (Wolfe et al., 1979; Love and Rotheim, 1984). We examined the expression of mating-type proteins, MTA and MTB, which are required for pair formation (Cervantes et al., 2013). In the starved wild-type cells having the same mating type as FAP256-KO cells (B mt IV), MTA4-GFP was detected in the anterior cell cortex, whereas MTB4-GFP was enriched near the anterior cell pole

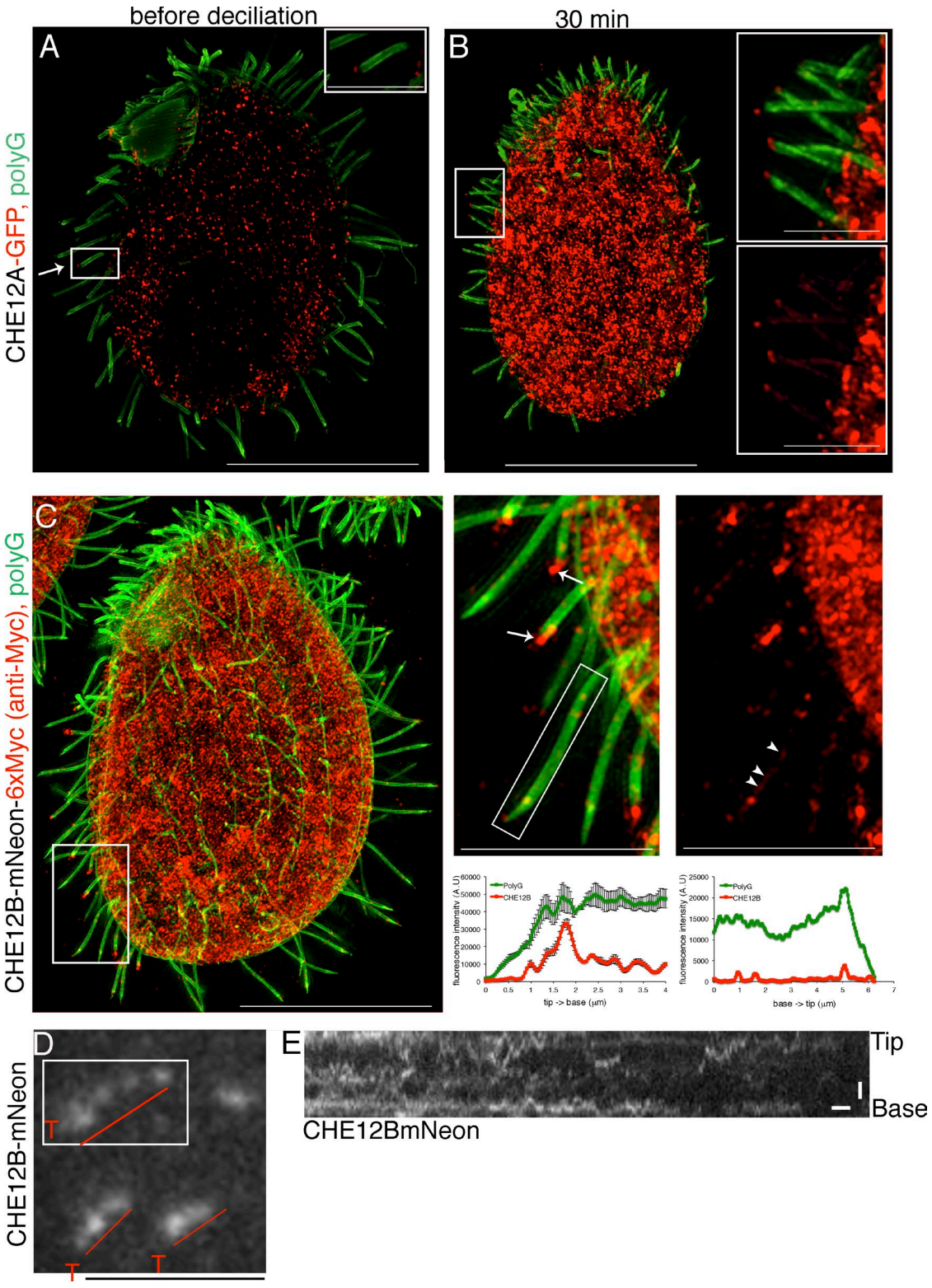

Figure 2. **CHE12 localizes near the ends of B-tubules. (A and B)** SR-SIM immunofluorescence imaging of CHE12A-GFP in growing cells before and 30 min after low pH–induced deciliation (during cilia regeneration; green, polyG tubulin; red, anti-GFP; bars: 20 µm [main], 5 µm [inset]). In A, the arrow shows a short (growing) cilium with CHE12A-GFP at the tip. Such cilia are numerous in the cell after deciliation during cilia regeneration (B). **(C)** An SR-SIM immunofluorescence image of CHE12B-mNeon-6xMyc (green, polyG tubulin; red, 6xMyc; bars: 20 µm [main], 10 µm [inset]). White arrow points to CHE12B at the ciliary tip. The graph shows average fluorescence intensity over the cilium length (error bars are standard deviations, $n = 4$ cilia; A.U., arbitrary units). White arrowheads mark the punctate signals along the cilium shaft. **(D)** A single TIRFM image frame taken from Video 2. The positions of three ciliary shafts are outlined by red lines, and the tips of these cilia are marked with red Ts (bar, 5 µm). **(E)** A kymograph corresponding to a single cilium (inside the box in D) reveals that CHE12B undergoes diffusion (bars, 1 µm and 1 s).

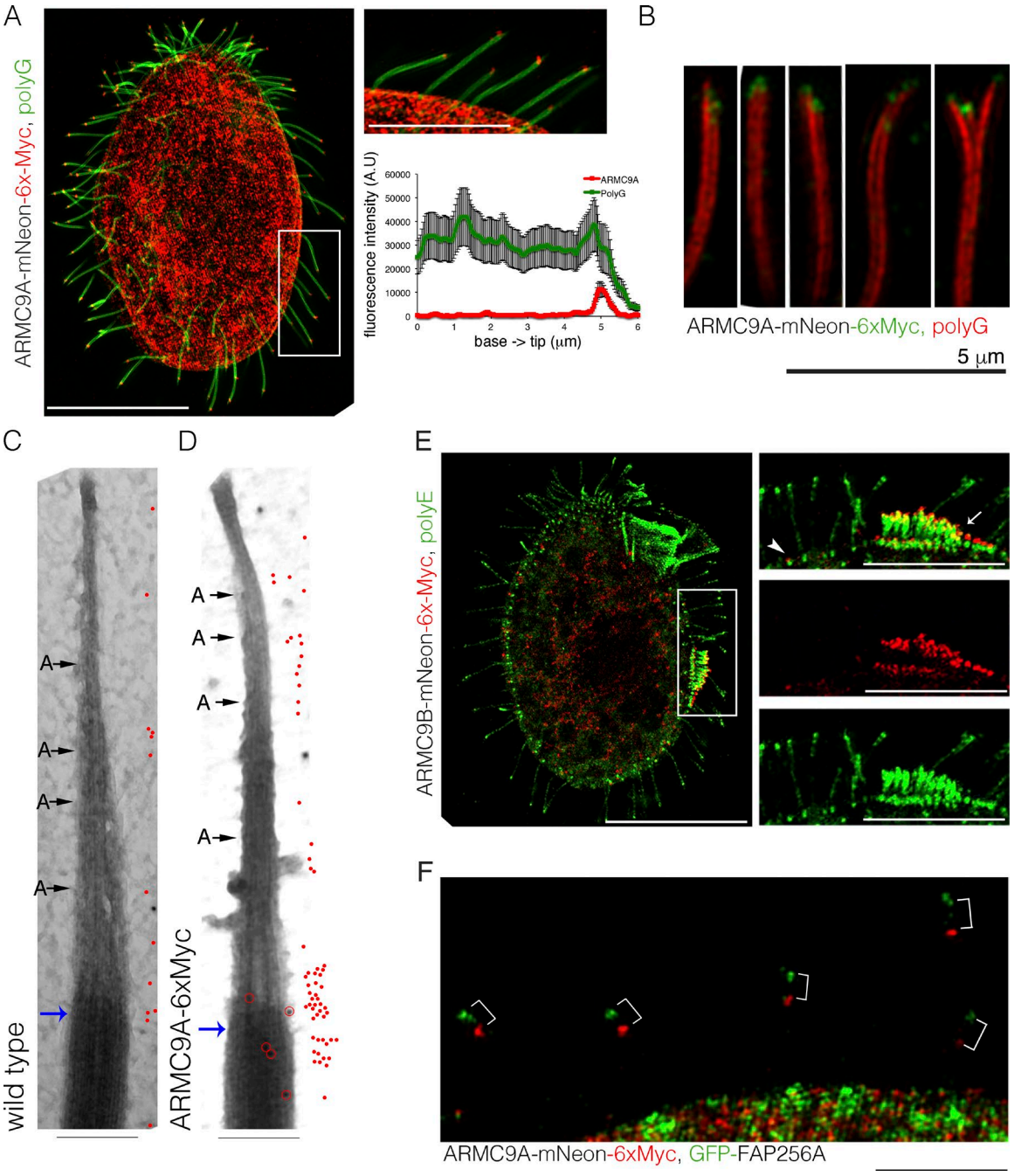

Figure 3. **ARMC9 localizes near the ends of B-tubules. (A)** An SR-SIM immunofluorescence image of ARMC9A-mNeon-6xMyc. The cell was labeled with polyG tubulin (green) and anti-Myc (red) antibodies (bars: 20 µm [main], 10 µm [inset]). ARMC9A is associated with the tips of mature full-length cilia; the graph shows the average fluorescence intensity along the cilium length (error bars show standard deviations, *n* = 3 cilia; A.U., arbitrary units). **(B)** SR-SIM images of isolated cilia (of cells expressing ARMC9A-mNeon-6xMyc) that have partially splayed microtubules (red, polyG tubulin; green, 6xMyc). **(C and D)** Immunogold TEM localization of ARMC9A in cilia of wild-type (C) and ARMC9A-mNeon-6xMyc expressing cells (D) using an anti-Myc primary antibody. The red circles mark the gold particles on the axonemes. The red dots on the right side summarize the distribution of gold particles at these approximate positions in a total of 18 cilia per genotype. The blue arrows mark the proximal boundary of distal segment and the As mark the termination points of identifiable A-tubule ends (note that some of these ends could be on the nonimaged side of the axoneme or were lost during preparation (bars, 200 nm). **(E)** An SR-SIM image of a cell expressing ARMC9-2xmNeon-6xMyc labeled with anti-Myc (red) and polyE (green) antibodies. ARMC9B is associated with the tips of assembling cilia. The box marks growing cilia of the assembling new oral apparatus (bars: 20 µm [main]; 10 µm [inset]). **(F)** An SR-SIM image of a portion of a *Tetrahymena* cell coexpressing MTT1-driven GFP-FAP256A (green, GFP) and ARMC9A-mNeon-6xMyc (red, 6xMyc; the brackets connect the FAP256 and ARMC9 signals on the same cilia; bar, 5 µm).

and at the tips of some anterior cilia (Fig. S4, H and J). However, MTA4-GFP and MTB4-GFP were not detectable above the background in FAP256-KO cells (Fig. S4, I and K). The levels of MTA and MTB mRNAs were normal in FAP256-KO cells (Fig. S4 L). Thus, the loss of FAP256 reduces either the levels or the cortical presence of mating type proteins and this is sufficient to explain the deficiency in pair formation. To summarize, losses of three distal segment boundary proteins in *Tetrahymena* affect the

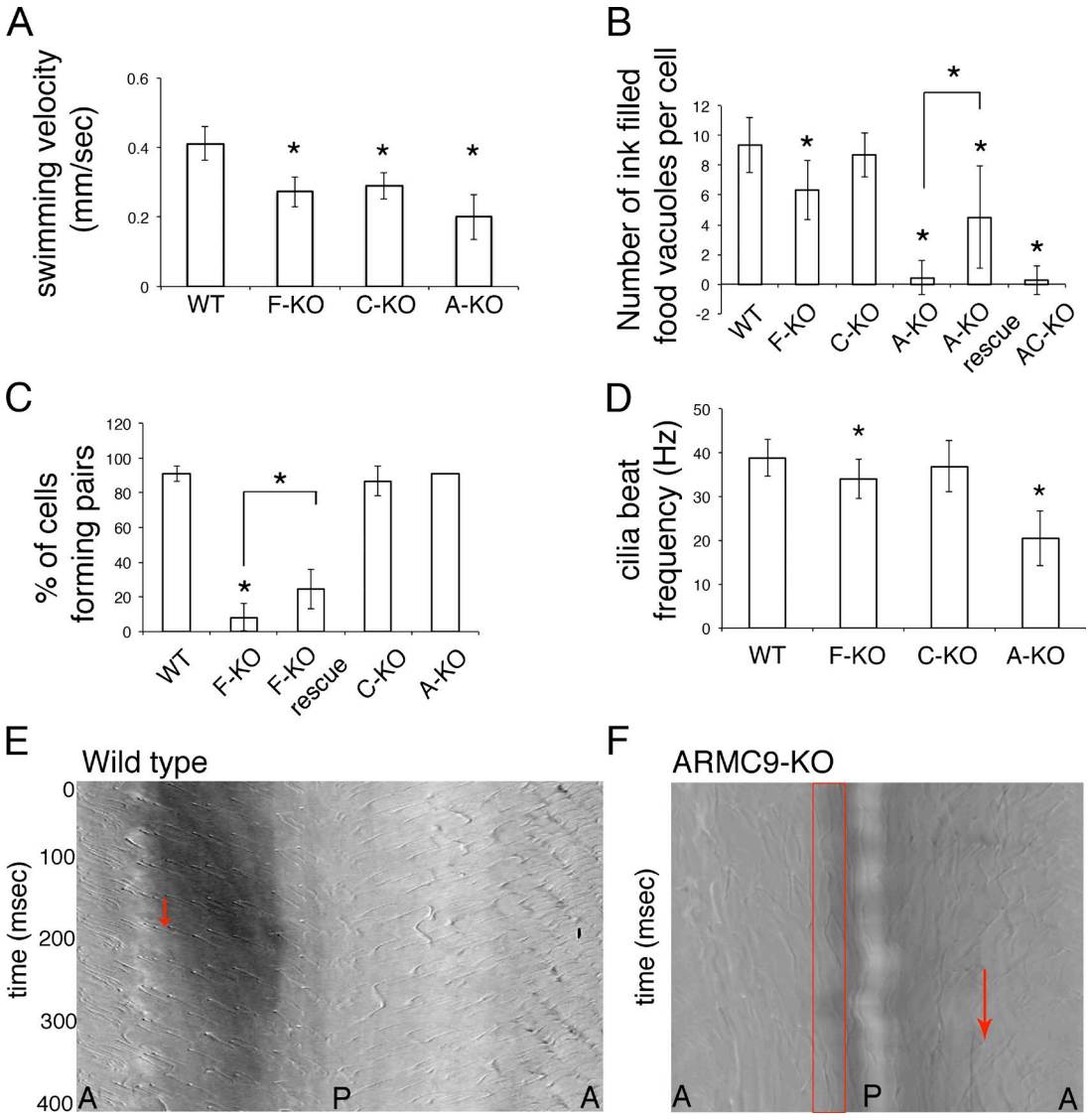

Figure 4. **Losses of FAP256, CHE12 and ARMC9 affect cilia. (A)** Swimming velocities of growing wild type (WT; 0.41 mm/s; *n* = 31), FAP256-KO (F-KO; 0.27 mm/s; *n* = 22), CHE12-KO (C-KO; 0.29 mm/s; *n* = 16), and ARMC9-KO (A-KO; 0.2 mm/s; *n* = 15) cells. The asterisks mark significant differences as compared with the wild type (two-sided *t* test, P < 0.001). **(B)** The rates of phagocytosis expressed as the number of ink-filled food vacuoles per cell after 10 min of exposure to india ink (asterisks show significant differences as compared with wild type; *n* = 50 cells; two-sided *t* test, P < 0.05). **(C)** Rates of pair formation. Wild-type or KO cells were mixed with an equal number of wild-type cells of a complementary mating type, and the percentage of cells in pairs was scored 6 h later (asterisks show significant differences compared with the wild-type cross; *n* = 100 cells; two-sided *t* test, P < 0.05). **(D)** Ciliary beat frequencies of wild type (39.8 ± 4.2 Hz, *n* = 109), FAP256-KO (34 ± 4.4 Hz, *n* = 58), CHE12-KO (37 ± 5.8 Hz, *n* = 95 cilia), and ARMC9-KO cells (20.5 ± 6.2 Hz, *n* = 37 cilia). Error bars represent standard deviations, asterisks indicate statistical significance compared with the wild type (two-sided *t* test, P < 0.05). **(E and F)** Space-time diagrams that document ciliary motility based on the Videos 3 and 6. Using a Matlab application, the area around the cell containing cilia was extracted as a video, unfolded, and used to create a space-time diagram. The x axis represents the position of cilia along the *Tetrahymena* cell surface (A, anterior; P, posterior end of the cell). The y axis represents time in milliseconds. Each short diagonal line represents a single cilium moving along the cell surface over time. The red arrows mark an example of a single beat cycle, and the red rectangle marks an example of a paralyzed cilium.

parameters of cilia (number, length, and beat parameters) and reduce cilia-dependent functions. While ARMC9 is particularly important for ciliary motility, FAP256/CEP104 may have a role in the cilia-based cell–cell signaling associated with conjugation.

FAP256 is important for capping of CP microtubules, and ARMC9 affects the middle segment organization

The ends of all axonemal microtubules that have complete tube walls (A-tubules and CP) carry ciliary caps, structures which plug the microtubule ends and connect them to the ciliary plasma membrane (Fisch and Dupuis-Williams, 2011). The A-tubule ends have carrot-like distal filaments (DFs), and the central microtubules end with the large central microtubule cap (CMC; Fig. 1 A; Dentler and Rosenbaum, 1977; Sale and Satir, 1977; Dentler, 1980). Based on the negatively stained isolated axonemes, in the wild type, the CMC was present at the end of almost every CP examined (Fig. 5 A). While the CMC frequency was not affected by the loss of either CHE12 or ARMC9, it was missing in most (92%, *n* = 76) of FAP256-KO axonemes (Fig. 5, A–D). Because CMC is present in some of FAP256-KO axonemes, FAP256 is not required

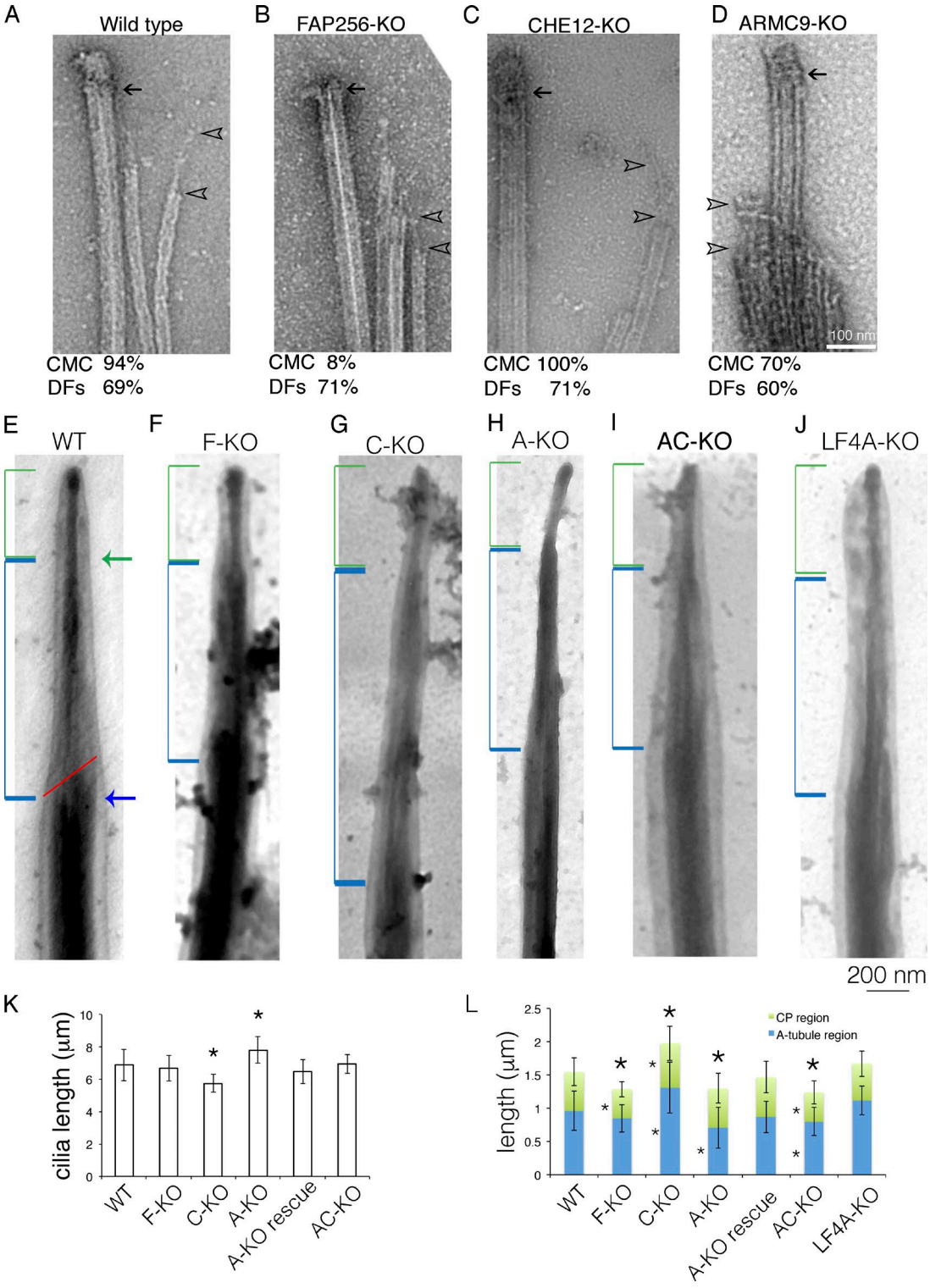

Figure 5. **FAP256, CHE12, and ARMC9 affect the dimensions of distal segment and FAP256 is needed for assembly or stability of the CMC. (A–D)** Images of negatively stained wild-type and KO axonemes. Arrows point to the ends of the CP microtubules (the location of the CMC), and arrowheads mark the proximal and distal ends of the DFs. The percentage of axonemes with ciliary caps are shown below each image (wild-type CMC score $n = 48$, DFs $n = 19$; FAP256-KO CMC $n = 76$, DFs $n = 42$; CHE12-KO CMC $n = 11$, DFs $n = 7$; and ARMC9-KO CMC $n = 10$, DFs $n = 10$). **(E–J)** Representative electron microscopy images of negatively stained whole mount wild-type and KO cilia (blue and green brackets mark the A-tubule and CP region, respectively; the blue and green arrows mark the proximal boundary of the distal segment and CP region, respectively; the red line indicates the region of decreased stain on the axoneme that corresponds to the termination of dynein arms and radial spokes on the A-tubules; see Fig. S5 [I–K] for the cross sections along the transitional region). **(K)** Cilium length was quantified using electron microscopic images of negatively stained isolated cilia (WT: 6.9 µm, ±0.97 $n = 51$; C-KO: 5.8 µm, ±0.57, $n = 39$; F-KO: 6.7 µm, ±0.79, $n = 49$; A-KO: 7.8 µm, ±0.82 $n = 70$; and AC-KO: 6.9 µm, ±0.57 $n = 50$, asterisks show significant differences compared with wild type;

for the CMC presence, but it may contribute to its assembly or stability. Although the DFs are more difficult to discern, one or more were visible at the ends of A-tubules in most wild-type and mutant axonemes (Fig. 5, A–D).

We have not encountered abnormalities in the middle (doublet) segment of FAP256-KO and CHE12-KO cilia. A small fraction (7%, n = 62) of ARMC9-KO cilia cross sections lacked (partially or completely) outer dynein arms (Fig. S5, A and B). Other infrequent abnormalities in ARMC9-KO included doublet microtubules that were broken or appeared to have split subfibers (Fig. S5, C–H).

FAP256, CHE12, and ARMC9 contribute to the geometry of the distal segment

Based on their localizations near the ends of axonemal microtubules, the three proteins may affect the positions of microtubule ends and thus influence the distal segment dimensions. The loss of FAP256 did not affect cilium length (Fig. 5 K) but caused a significant reduction in the length of distal segment (by ∼248 nm), by shortening both the A-tubule region (by ∼95 nm) and the CP region (by ∼142 nm; Fig. 5, F and L). A part of the effect on the CP region length is the loss of the CMC bead (Fig. 5, A and B) that is ∼100 nm in size (Sale and Satir, 1977). While the entire cilium length did not change significantly, a shortening of distal segment by ∼250 nm would fall within the standard deviation of the wild-type total length value. Likely, in the absence of FAP256, both the distal segment and consequently the entire cilium shorten by ∼250 nm. Remarkably, overexpression of GFP-FAP256A significantly shortened the CP region without affecting the total length of distal segment (Fig. 6 A, B, and D), which is consistent with elongation of A-tubules. In many cilia of cells overproducing GFP-FAP256A, the ends of A-tubules were positioned immediately below the CMC (Fig. 6 B). Taking the loss- and gain-of-function data together, FAP256 elongates A-tubules, and stabilizes the CMC. Surprisingly, in the cell body, overexpressed GFP-FAP256A formed long tubulin-free fibers consistent with its oligomerization at higher concentration (Fig. S1 D and see Discussion).

In the absence of CHE12, the entire cilium was shorter by ∼1.1 µm (16%; Fig. 5 K). Remarkably, the distal segment, and within it the A-tubule and CP regions, were ∼530 nm, ∼366 nm, and ∼146 nm longer, respectively (Fig. 5, G and L). These changes are consistent with shortening of all microtubules, with the B-tubules being relatively more affected. Collectively with the localization near the B-tubule ends, CHE12 most likely promotes elongation of B-tubules. Possibly the shortening of complete microtubules (A-tubules and CP, and consequently the entire cilium) is secondary to the shortening of B-tubules (see below).

In the ARMC9-KO strain of *Tetrahymena*, cilia were longer by ∼0.93 µm (14%; Fig. 5 K). However, the entire distal segment and the A-tubule region were reduced by ∼200 nm and ∼185 nm, respectively, whereas the CP region was unaffected (Fig. 5, H and L). Thus, in ARMC9-KO, the B-tubules were excessively long in relation to the A-tubules. An introduction of GFP-ARMC9B into ARMC9-KO cells rescued the abnormal geometry of distal segment (Fig. 5 L). Strikingly, overexpression of GFP-ARMC9B made the distal segment longer (by ∼30%), indicating that ARMC9 has activity that shortens the B-tubules (Fig. 6, C and E–G).

CHE12 and ARMC9 affect both the geometry of distal segment and the total cilium length (consistently in opposite ways; see the summary of *Tetrahymena* KO phenotypes in Table S4), opening a possibility that the distal segment defects are secondary to the cilium length defects. To test whether there is a correlation between cilium and distal segment length, we examined a *Tetrahymena* strain lacking LF4A (TTHERM_00058800), an orthologue of cilium length regulators, LF4/MOK kinases (Berman et al., 2003). While the LF4A-KO cilia are 30% longer (unpublished data), the lengths of entire distal segment and its subregions were normal (Fig. 5, J and L). Thus, an increase in cilium length can occur without a change in the dimensions of the distal segment (solely by elongation of the middle segment). This argues that the defects in the distal segment dimensions observed in the ARMC9 and CHE12 mutants are not secondary to an abnormal cilium length.

Because ARMC9 and CHE12 have a negative and positive effect on the B-tubule length, respectively, we disrupted both gene families in one strain to test for interactions. The ARMC9_CHE12-KO double KO cells grew and fed as poorly as the single KO ARMC9-KO (Fig. 4 B). However, the length of ARMC9_CHE12-KO cilia was normal (Fig. 5 K). This additive effect on the cilium length indicates that ARMC9 and CHE12 act in two competing pathways. However, in other aspects the ARMC9-KO phenotype masked the CHE12-KO phenotype, including the multiplication and phagocytosis rates. Furthermore, the distal segment and A-tubule region were 305-nm and 141-nm shorter than the wild type, respectively, and similar to the values of ARMC9-KO (Fig. 5, H, I, and L). Thus, the ARMC9_CHE12-KO cilia are functionally severely deficient, despite having a normal overall length. This further argues that the disturbed organization of the distal segment is the cause of ciliary functional defects in the absence of ARMC9 and CHE12.

Discussion

Sizing mechanisms must operate not only at the whole cell and organelle level, but also inside organelles, including those built around microtubules, such as cilia. Despite the discovery of factors that promote either microtubule assembly or disassembly (Akhmanova and Steinmetz, 2015; Bowne-Anderson et al., 2015), how the sizes of microtubules are coordinated within a group remains unknown. The ciliary distal segment offers a rare opportunity to address the mechanism of sizing of microtubules within a functional group. We show that three conserved proteins are enriched either at the distal (FAP256/CEP104) or proximal (CHE12 and ARMC9) boundary of ciliary distal segment, and regulate its

two-sided t test, P < 0.05). **(L)** Quantifications of the length of distal segment, A-tubule and CP region (averages ± standard deviations, n = 40–70 cilia, asterisks show significant differences as compared with the wild type; two-sided t test, P < 0.05; * at the top of the column shows a significant difference in the distal segment; * on the side of each column shows a significant difference in either the CP [top] or the A-tubule region [bottom]).

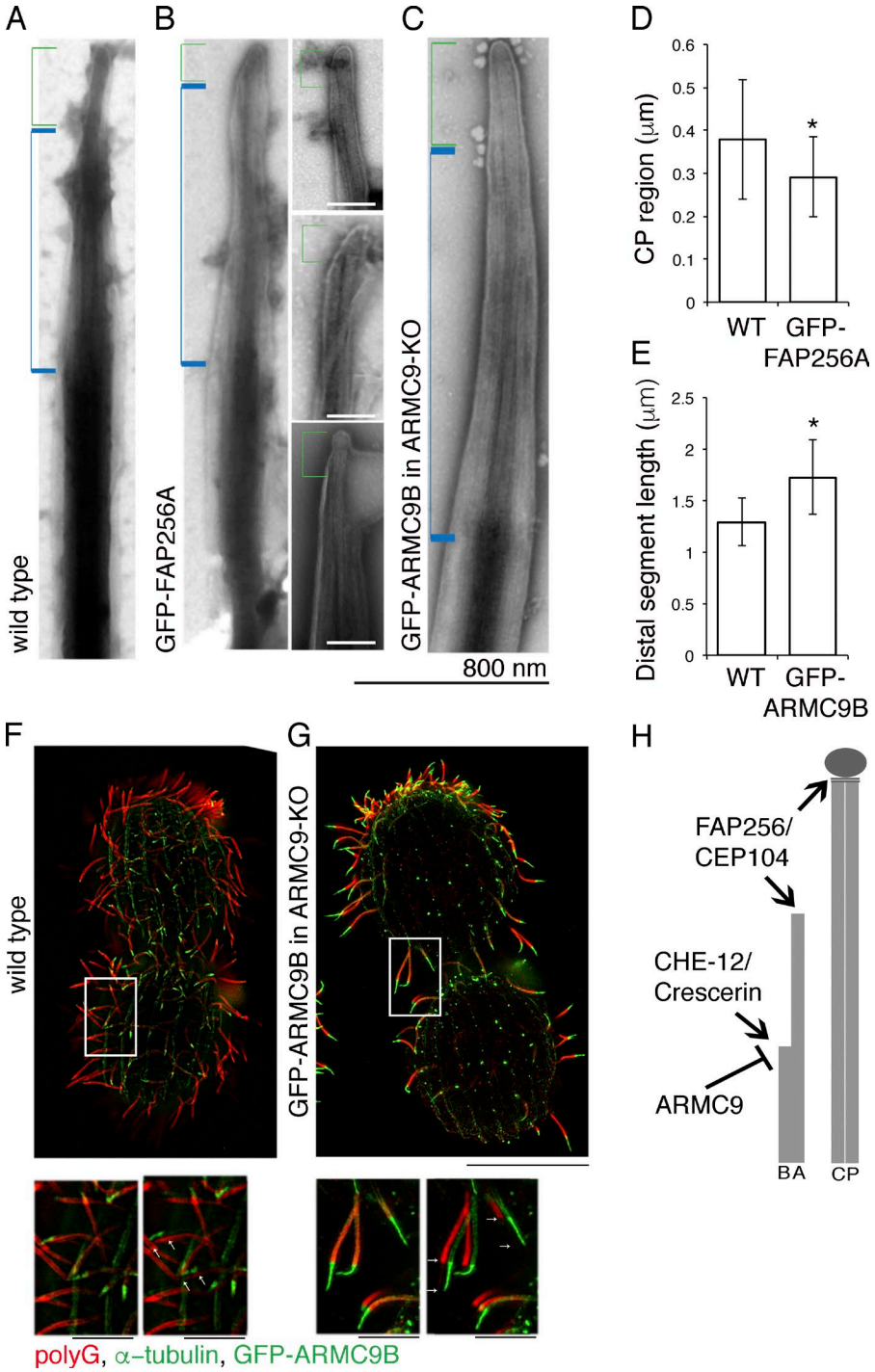

Figure 6. **FAP256 activity elongates the A-tubules while ARMC9 activity shortens the B-tubules. (A–C)** Negatively stained whole cilia from a wild type (A) and cells overproducing either GFP-FAP256A (B; inset bar, 100 nm) or GFP-ARMC9B (C) after 6 h of exposure to cadmium chloride to induce the transgenes (green bracket, CP region; blue bracket, A-tubule region). **(D and E)** Quantifications of the length of CP-region (n = 50–60) and distal segment (n = 45–67) based on the images of negatively stained whole cilia in cells overexpressing either GFP-FAP256A (D) or GFP-ARMC9B (E) for 6 h (mean ± standard deviation; two-sided t test, $P < 0.05$). **(F and G)** SR-SIM images of a wild type (F) and a GFP-ARMC9B overproducing cell (in the ARMC9-KO background; G) after 6 h of exposure to cadmium chloride to induce the transgene overexpression (green, α-tubulin detected by 12G10 monoclonal antibody and GFP-ARMC9B; red, polyG antibodies; bars: 20 µm [main], 5 µm [inset]). The anti–α-tubulin 12G10 antibody labels more strongly the distal segment (as compared with the middle segment) likely due to increased accessibility of microtubules not covered by motility-related complexes. Color channels are shifted in magnified images, arrows point to the boundaries of the distal segment. **(H)** A summary of the functions of FAP256/CEP104, CHE-12/Crescerin, and ARMC9 uncovered in this study.

dimensions by controlling the lengths of specific microtubule types. While FAP256 acts on the ends of complete microtubules (A-tubules) and promotes their elongation, CHE12 and ARMC9 act on the ends of B-tubules and mediate their elongation and shortening, respectively (Fig. 6 H). Thus, the distal segment geometry involves differential regulation of the ends of complete and incomplete microtubules. FAP256/CEP104 and CHE-12/Crescerin likely act by promoting addition of tubulin subunits to the ends of microtubules, an activity that is already well documented for another TOG domain plus end–tracking protein, XMAP215/DIS1/STU2 that elongates cytoplasmic and mitotic microtubules (Brouhard et al., 2008; Widlund et al., 2011; Ayaz et al., 2012, 2014; Fox et al., 2014).

FAP256/CEP104 and CHE-12/Crescerin could be directly targeted to the plus ends of either complete (A-tubules) or incomplete (B-tubules) axonemal microtubules, respectively. The lattices of A- and B-tubules have distinct protofilament curvatures (Ichikawa et al., 2017). In the case of CHE-12/Crescerin (Das et al., 2015), the relative positions of its multiple tubulin-binding TOG domains may confer the preferential docking onto the microtubule lattice with the B-tubule curvature. While FAP256/CEP104 has only a single TOG domain, our observation

that overproduced FAP256A forms long fibers opens a possibility that FAP256 oligomerizes on the microtubule surface, in analogy to the mitotic plus end–tracking proteins, NDC80 and Dam1 (Westermann et al., 2005; Alushin et al., 2010). An oligomerization of FAP256/CEP104 may contribute to its preferential recognition of the ends of complete microtubules (A-tubules and CP), and promote its persistence on the microtubule surface to allow it to remain at the tips of growing, steady-state and disassembling cilia (Satish Tammana et al., 2013).

CHE12 and ARMC9 compete to regulate the B-tubule length. ARMC9 may be a signaling protein (Van De Weghe et al., 2017; Breslow et al., 2018; Kar et al., 2018) that either activates a microtubule end depolymerizer or inhibits a polymerization factor. Neither ARMC9 nor CHE12 are absolutely required for the generation of a recessed microtubule end, but rather act as regulators whose activities control the positions of the microtubule ends and regulate the length of distal segment.

It is intriguing that the losses of CHE12 and ARMC9 also affect overall cilium length in a manner consistent with their effects on B-tubules. Since CHE12 and ARMC9 act on the ends of B-tubules, they are unlikely to directly regulate the cilium length, as this parameter is defined by the length of the CP (or A-tubules in 9+0 cilia). It seems more likely that the effects of CHE12 and ARMC9 on cilium length are secondary due to the changes in the B-tubules. Within the middle segment, the B-tubules are the main if not exclusive track for the anterograde IFT (Stepanek and Pigino, 2016), an activity that delivers the building blocks needed for cilium assembly. It needs to be mentioned that in the mammalian 3T3 cell line that expresses an sgRNA targeting ARMC9, cilia are excessively short. Strikingly, in the IMCD3 cells in which Hh signaling was stimulated, ARMC9 accumulates at the ciliary tip (Breslow et al., 2018). Thus, the observations made in both *Tetrahymena* and mammalian cells, link ARMC9 to cilium length regulation and the ciliary tip, and it remains to be determined whether its role as a negative regulator of the B-tubule length is also conserved in mammals.

The distal segment lacks motility-associated protein complexes including dynein arms and radial spokes. Thus, it is unexpected that cilia in *Tetrahymena* cells lacking either FAP256/CEP104 or ARMC9 are deficient in ciliary motility. In *Tetrahymena*, in the absence of FAP256, most of the ends of central microtubules lack the CMC, in agreement with the abnormally blunt ciliary tips reported in the *Chlamydomonas* mutant lacking FAP256 (Satish Tammana et al., 2013). Possibly, in addition to its role in promoting complete microtubule elongation, FAP256 acts as a linker to reinforce the external portion of the CMC at the microtubule end. The spherical shape of the CMC bead may facilitate the twisting of the CP (Fisch and Dupuis-Williams, 2011), and this may be important for the waveform bend propagation (Omoto and Kung, 1979, 1980; Omoto et al., 1999; Mitchell, 2003). Surprisingly the ciliary beat frequency and waveform are not affected in the CHE12 KO cilia despite their shorter middle segment and the corresponding reduction in the number of dynein arms. In contrast, cilia lacking ARMC9 have a longer force-producing middle segment, but display severe defects in the beat frequency and waveform. The altered organization of the distal segment could affect ciliary motility either through changes in the physical properties of the distal portions of microtubules or by disturbing regulatory proteins (see below) that may selectively recognize the singlet microtubules or the plus-ends of microtubules. Additionally, infrequent structural defects in the middle segment of ARMC9-KO cilia (including fewer dynein arms) could reflect axoneme assembly errors that may reduce ciliary motility.

A growing body of evidence links the tips of sensory primary cilia to essential signaling during mammalian development. Defects in the Hh signaling are associated with a failure of Hh signaling molecules, Gli and Sufu, to concentrate at the ciliary tip (Haycraft et al., 2005; Liem et al., 2009; Tukachinsky et al., 2010). Intriguingly, the length of distal segment is dynamic; in *Chlamydomonas*, the distal segment is relatively short in vegetative cells and elongates during mating, and this correlates with ciliary accumulation of molecules involved in cell-cell adhesion (Mesland et al., 1980). We show that a loss of FAP256 in *Tetrahymena* decreases pair formation, a process that involves cell–cell communication (Wolfe et al., 1979; Love and Rotheim, 1984). In humans, mutations in FAP256 and ARMC9 cause Joubert syndrome (Srour et al., 2015; Van De Weghe et al., 2017; Kar et al., 2018), a ciliopathy with mostly neurological defects. None of the Joubert syndrome proteins are directly associated with ciliary motility, suggesting that defects in the sensory primary cilia cause the disease. The Joubert syndrome proteins described to date localize to either the basal body, transition zone or notably to the ciliary tip (Shaheen et al., 2016). Here we link two Joubert syndrome proteins, FAP256 and ARMC9, to the ends of specific axonemal microtubules within the distal segment. Additional ciliary tip proteins whose mutations causes Joubert syndrome are KIF7 (Dafinger et al., 2011; He et al., 2014) and KIAA0556 (Sanders et al., 2015). KIF7 may contribute to the distal segment organization by shortening the ends of axonemal microtubules (He et al., 2014). Interestingly, a loss of KIA0566 in *C. elegans* produces longer cilia with fewer A-tubules and occasionally doublet microtubules at the position normally occupied by the distal segment (Sanders et al., 2015), a partial phenocopy of the loss of ARMC9 described here. Thus, mutations in ciliary tip proteins may cause Joubert syndrome by changing the organization of the distal segment.

Materials and methods

Tetrahymena strains, culture, and gene editing

Tetrahymena thermophila strains were grown at 30°C in either SPP (Gorovsky, 1973) or MEPP (Orias and Rasmussen, 1976) media with antibiotics (Dave et al., 2009). CU428 strain was used as a wild type (*Tetrahymena* Stock Center). Homologous DNA recombination was used to add sequences encoding epitope tags (GFP or 2xmNeonGreen-6xMyc-BirA*; Shaner et al., 2013) to the ends of predicted open reading frames (ORFs) in the native loci, or complete ORFs were inserted into *BTU1* locus for overexpression under the cadmium-inducible *MTT1* promoter (Dave et al., 2009; Gaertig et al., 2013). The primers used to amplify fragments of genes for tagging the native loci are listed in Table S1. Micronuclear strains with disruptions of *FAP256A* (*TTHERM_00079820*), *FAP256B* (*TTHERM_00584800*), *CHE12A* (*TTHERM_00102840*), *CHE12B* (*TTHERM_00193480*), *ARMC9A*

(*TTHERM_00723450*), and *ARMC9B* (*TTHERM_0042850*) genes were made by replacing a part of each ORF with *neo4* (Mochizuki, 2008) or *bsr2* (Couvillion and Collins, 2012) cassettes by biolistic transformation (Cassidy-Hanley et al., 1997; Dave et al., 2009). The KO phenotype-expressing homokaryon strains were produced by mating of heterokaryons (Hai et al., 1999). The losses of the targeted fragments were confirmed by PCR using primers specific to the deleted sequences. The primers used to amplify the homology arms for gene targeting and to confirm the losses of targeted sequences are listed in Table S1.

Microscopic analyses of *Tetrahymena*

Cells were fixed/permeabilized using 2% paraformaldehyde and 0.5% Triton X-100 in the PHEM buffer, dried, rehydrated in the phosphate-buffered saline with 3% bovine serum albumin and 0.01% Tween-20 and stained with antibodies as described (Gaertig et al., 2013), using one or more of the following reagents: DAPI (Sigma-Aldrich; 0.5 µg/ml), antibodies directed to: α-tubulin (12G10 [mouse monoclonal], 1:30 dilution; Developmental Hybridoma Bank; Jerka-Dziadosz et al., 2001), polyglycylation (polyG, 2302 serum [rabbit], 1:200; Duan and Gorovsky, 2002), polyglutamylation (polyE, 2304 serum [rabbit], 1:100; Shang et al., 2002), centrin (20H5 [mouse monoclonal], 1:100; Salisbury et al., 1988), Myc (9E10 [mouse monoclonal]; Developmental Hybridoma Bank, undiluted), or GFP (abcam6556; rabbit polyclonal, 1:100). Fixed cells were incubated with antibodies overnight at 4°C. The secondary antibodies conjugated to either FITC or Cy3 (Zymed Laboratories) were used at 1:250 (1-h incubation at room temperature). Fluorescence imaging was performed either on a Zeiss LSM 710 confocal (using the 63× Plan-Apochromat objective) or Zeiss ELYRA S1 SR-SIM microscope (with the Plan-Apochromat 100×/1.46 objective). The SR-SIM images were collected on an AxioCam HSm charge-coupled device camera (operated with Axiovision software) and analyzed by National Institutes of Health ImageJ (Schneider et al., 2012). The TIRFM was performed after immobilization of cells with nickel chloride exactly as described (Jiang et al., 2015b). The density of cilia on the cell surface was calculated as the average number of cilia per micrometer on a confocal slice containing the widest cell circumference. The regeneration of cilia was observed after deciliation as described (Calzone and Gorovsky, 1982).

Thin sections were analyzed by TEM as described (Urbanska et al., 2015). To negatively stain isolated cilia, *Tetrahymena* cells were deciliated with dibucaine or low pH (Gaertig et al., 2013), and cilia were purified and negatively stained with 1% or 1.5% uranyl acetate (Suprenant and Dentler, 1988). To visualize the ciliary caps, purified cilia were extracted with 1% NP-40 in 50 mM Tris, pH 7.4, 3 mM $MgSO_4$, 0.1 mM EGTA, 0.25 M sucrose, and 1 mM DTT for 10 min; centrifuged; suspended in 50 mM Pipes, pH 7.10, 3 mM $MgSO_4$, 0.1 mM EGTA, 0.25 M sucrose, 1 mM DTT, and 1 mM phenylmethylsulfonyl fluoride; and observed in a FEI Technai F20XT electron microscope. To measure the length of the distal segment, whole cells were fixed with 2% paraformaldehyde in PHEM buffer (Gaertig et al., 2013), placed on formvar-coated grids and stained with 1.5% uranyl acetate. Images were collected on a JEOL JEM1011 electron microscope. Cilia that had an intact membrane and well-stained axonemes were used for measurements of the length of the distal segment using NIH ImageJ (Schneider et al., 2012). Such cilia were inspected in the longitudinal view. Straight lines were drawn that were the best fits for most of the cilium length along the two edges of the plasma membrane. The cilium was then inspected from the base to the tip. The width position at which the plasma membrane tapers off from the cilium edge lines was designated as the proximal boundary of the distal segment. As an additional marker, within the same region, the axoneme reduces its stain intensity due to the termination of dynein arms and radial spokes. This forms a slightly oblique pattern, because not all B-tubule termination points are at the same level (Fig. 5 E and Fig S5, I–M; Sale and Satir, 1976; Dentler, 1980). Above the distal segment boundary, the axoneme width gradually decreases due to the termination of the A-tubules (at multiple positions) followed by the termination of the CP microtubules. The width position at which the axoneme becomes maximally thin was designated as the proximal boundary of the "CP region" that contains only central microtubules.

Phenotypic studies of *Tetrahymena*

The cell swimming velocity was measured using 30-s video recordings of growing cells (1 ml at 10^4 cells/ml in a well of a 24-well plate,) using an AxioCam HS camera mounted on a Nikon Observer.A1 microscope with a 10× lens. The velocities were calculated using AxioVision software (Zeiss). The ciliary beat frequency was measured in *Tetrahymena* cells swimming in a microfluidic channel on an inverted microscope (Nikon TE2000) with a 60× objective lens. Videos were recorded using a Photron 1024PCI camera at 2,000 fps. The observation area was a section of a long straight channel (33 µm in height and 50 µm in width). The cells were injected into the inlet of the channel using a controllable pressure source (Fluigent), after which the pressures between the inlet and outlet were equilibrated, to prevent residual flow. The calculation of ciliary beat frequency was done as described (Funfak et al., 2015). In brief, a Matlab code was used to track the moving cell and align a series of consecutive images at the same position relative to the internal cell body markers (as if the cell was not moving). This "composite cell" was digitally unwrapped to produce a rectangular segment around the cell's contour. A space-time mapping was used to produce a kymograph of ciliary-beating activity across the cell surface. The ciliary beat frequency was obtained by auto-correlation on the signal in each column of the kymograph and searching for the time of the first peak.

Proximity biotinylation and mass spectrometry in *Tetrahymena cilia*

A codon optimized (for *T. thermophila*) BirA* coding region (Roux et al., 2012) was added to the 5′ end of an ORF encoding NRK2(K35R)-GFP (Wloga et al., 2006), and the resulting fusion protein was expressed under *MTT1* promoter in the *BTU1* locus . The expression of BirA*-NRK2(K35R)-GFP and GFP-BirA* (also under *MTT1* promoter) was induced with 2.5 µg/µl $CdCl_2$ for 2 h in the presence of 50 µM biotin. Cilia were isolated after low pH shock deciliation (Gaertig et al., 2013) and solubilized in the lysis buffer (50 mM Tris, pH 7.4, 500 mM NaCl, 0.4% SDS, and 1 mM DTT) for 1 h at room temperature. The lysate was frozen in liquid

nitrogen and used for direct detection of biotinylated peptides by mass spectrometry (Schiapparelli et al., 2014). For every protein hit, a normalized spectral associate factor was calculated. The mRNA expression patterns were analyzed using Co-regulation Data Harvester (Tsypin and Turkewitz, 2017).

Quantification of mRNA levels by real-time quantitative PCR (qRT-PCR)

Total RNA was isolated from starved wild-type (B mt IV) and mutant (FAP256-KO) *Tetrahymena* cultures, and cDNA was prepared using iScript cDNA synthesis kit (Bio-Rad, Inc.). The data were analyzed using the Pfaffl method (Pfaffl, 2001). The primers used for qPCR are listed in Table S3.

Multiple sequence alignment

A multiple sequence alignment of CEP104/FAP256 was generated using ClustalW (Larkin et al., 2007; Goujon et al., 2010). The sequences used were from *Tetrahymena thermophila* gi|118365202, *Ichthyophthirius multifiliis* gi|471221679, *Paramecium tetraurelia* gi|145521394, *Oxytricha trifallax* gi|403345233, *Stylonychia lemnae* gi|678325194 and gi|678312996, *Saimiri boliviensis* gi|725596390, *Physcomitrella patens* gi|168045131, and *Homo sapiens* AAH01640.1.

Multiplication rates of *Tetrahymena* strains

Growing cultures of wild-type and KO strains were adjusted to 10^4 cells/ml, and cell concentration was periodically measured during 36 h ($n = 3$ independent experiments).

Online supplemental material

Fig. S1 (A–C) describes the domain organization and structure of the TOG domain of the *Tetrahymena* orthologues of FAP256/CEP104. Fig. S1 D displays images of cells overexpressing FAP256A-GFP. Fig. S2 (A and B) shows immunogold TEM images of cilia stained with polyG antibodies. Fig. S2 (C–K) contains representative TEM cross sections through the distal segment of wild-type cilia. The estimated positions of termination points of specific A-tubules within the distal segment are shown in Fig. S2 L. Fig. S2 M is a quantification of the cilium and axoneme circumferences through the middle and distal segment. Fig. S3 shows SR-SIM images documenting the localization of FAP256A and CHE12B in reference to the markers of the middle segment, polyG and polyE, respectively. Fig. S4 (A–G) contains fluorescence images of cells (obtained with the anti-centrin and anti-polyG antibodies), as well as graphs documenting the growth and phagocytosis rates of wild-type and KO strains. Fig. S4 (H–L) shows the localization and expression levels of the mating-type proteins, MTA and MTB, in the wild-type and FAP256-KO cells. Fig. S5 contains representative TEM images of wild-type and ARMC9-KO cilia. Videos 1 and 2 show a live TIRFM video of a cell expressing FAP256A-GFP and CHE12BmNeonGreen, respectively. Videos 3–6 are high speed videos of wild-type (Video 3), FAP256-KO (Video 4), CHE12-KO (Video 5), and ARMC9-KO (Video 6) cells freely swimming in microfluidic channels. Table S1 includes all primers used for amplification of coding sequences for tagging of the native loci, overexpression, gene disruptions and genotyping. Table S2 shows the distal segment-associated protein candidates with at least 10-fold enrichment in BirA*-NRK2-(K35R)-GFP as compared with GFP-BirA*-expressing cilia. Table S3 lists the primers used for quantification of gene expression by qRT-PCR. Table S4 summarizes all the defects caused by the loss of either FAP256, or CHE12 or ARMC9 in *Tetrahymena*.

Acknowledgments

We thank Mary Ard (Georgia Electron Microscopy facility at University of Georgia) for assistance with electron microscopy and Muthugapatti K. Kandasamy (Biomedical Microscopy Core facility at University of Georgia) for assistance with fluorescence microscopy. We thank Joseph Frankel (University of Iowa) for critical reading of the manuscript. We thank the following researchers for providing reagents: Martin A. Gorovsky (University of Rochester) for polyE and polyG antibodies and Joseph Frankel (University of Iowa) for 12G10 antibodies (available from the Developmental Studies Hybridoma Bank, University of Iowa).

The research reported in this publication was supported by the National Institutes of Health, including grants R01GM089912 and R21HD092809 (to J. Gaertig), R01GM110413 (to K. Lechtreck), P41GM103533 (to J.J. Moresco and J.R. Yates III), R01GM099820 (to C.G. Pearson), and R01GM098543 (to L.M. Rice). P. Louka was supported by a predoctoral fellowship from the American Heart Association (no. 16PRE27480028). J. Gaertig was also supported by intramural grants from the Office of Vice-President for Research and the Department of Cellular Biology at the University of Georgia. R.F.-X. Tomasi and C.N. Baroud were funded by the European Research Council grant 278248 Multicell. D. Wloga was funded by the Polish National Science Centre 2014/14/M/NZ3/00511 (Harmonia 6) grant.

The authors declare no competing financial interests.

Author Contributions: P. Louka, W. Dentler, and J. Gaertig conceived the project. P. Louka, K.K. Vasudevan, and M. Guha constructed and analyzed the *Tetrahymena* mutants. D.F. Galati and C.G. Pearson contributed to the analyses of *Tetrahymena* mutants. P. Louka, E. Joachimiak, D. Wloga, and W. Dentler performed electron microscopic studies. P. Louka, R.F.-X. Tomasi, C.N. Baroud, and P. Dupuis-Williams evaluated the cilia motility. P. Louka prepared and J.J. Moresco and J.R. Yates III analyzed the BioID samples by mass spectrometry. P. Louka and L.M. Rice performed protein structure predictions. P. Louka, Y.-Y. Jiang, and K. Lechtreck performed the TIRFM observations. J. Gaertig supervised the project. P. Louka and J. Gaertig wrote the manuscript. All authors discussed and edited the manuscript.

Submitted: 20 April 2018
Revised: 25 July 2018
Accepted: 31 August 2018

References

Akhmanova, A., and M.O. Steinmetz. 2015. Control of microtubule organization and dynamics: two ends in the limelight. *Nat. Rev. Mol. Cell Biol.* 16:711–726. https://doi.org/10.1038/nrm4084

Al-Jassar, C., A. Andreeva, D.D. Barnabas, S.H. McLaughlin, C.M. Johnson, M. Yu, and M. van Breugel. 2017. The Ciliopathy-Associated Cep104 Protein Interacts with Tubulin and Nek1 Kinase. *Structure.* 25:146–156. https://doi.org/10.1016/j.str.2016.11.014

Alushin, G.M., V.H. Ramey, S. Pasqualato, D.A. Ball, N. Grigorieff, A. Musacchio, and E. Nogales. 2010. The Ndc80 kinetochore complex forms oligomeric arrays along microtubules. *Nature.* 467:805–810. https://doi.org/10.1038/nature09423

Ayaz, P., X. Ye, P. Huddleston, C.A. Brautigam, and L.M. Rice. 2012. A TOG:αβ-tubulin complex structure reveals conformation-based mechanisms for a microtubule polymerase. *Science.* 337:857–860. https://doi.org/10.1126/science.1221698

Ayaz, P., S. Munyoki, E.A. Geyer, F.A. Piedra, E.S. Vu, R. Bromberg, Z. Otwinowski, N.V. Grishin, C.A. Brautigam, and L.M. Rice. 2014. A tethered delivery mechanism explains the catalytic action of a microtubule polymerase. *eLife.* 3:e03069. https://doi.org/10.7554/eLife.03069

Bacaj, T., Y. Lu, and S. Shaham. 2008. The conserved proteins CHE-12 and DYF-11 are required for sensory cilium function in Caenorhabditis elegans. *Genetics.* 178:989–1002. https://doi.org/10.1534/genetics.107.082453

Berman, S.A., N.F. Wilson, N.A. Haas, and P.A. Lefebvre. 2003. A novel MAP kinase regulates flagellar length in Chlamydomonas. *Curr. Biol.* 13:1145–1149. https://doi.org/10.1016/S0960-9822(03)00415-9

Bowne-Anderson, H., A. Hibbel, and J. Howard. 2015. Regulation of Microtubule Growth and Catastrophe: Unifying Theory and Experiment. *Trends Cell Biol.* 25:769–779. https://doi.org/10.1016/j.tcb.2015.08.009

Breslow, D.K., S. Hoogendoorn, A.R. Kopp, D.W. Morgens, B.K. Vu, M.C. Kennedy, K. Han, A. Li, G.T. Hess, M.C. Bassik, et al. 2018. A CRISPR-based screen for Hedgehog signaling provides insights into ciliary function and ciliopathies. *Nat. Genet.* 50:460–471. https://doi.org/10.1038/s41588-018-0054-7

Brouhard, G.J., J.H. Stear, T.L. Noetzel, J. Al-Bassam, K. Kinoshita, S.C. Harrison, J. Howard, and A.A. Hyman. 2008. XMAP215 is a processive microtubule polymerase. *Cell.* 132:79–88. https://doi.org/10.1016/j.cell.2007.11.043

Calzone, F.J., and M.A. Gorovsky. 1982. Cilia regeneration in Tetrahymena. A simple reproducible method for producing large numbers of regenerating cells. *Exp. Cell Res.* 140:471–476. https://doi.org/10.1016/0014-4827(82)90144-6

Cassidy-Hanley, D., J. Bowen, J.H. Lee, E. Cole, L.A. VerPlank, J. Gaertig, M.A. Gorovsky, and P.J. Bruns. 1997. Germline and somatic transformation of mating Tetrahymena thermophila by particle bombardment. *Genetics.* 146:135–147.

Cervantes, M.D., E.P. Hamilton, J. Xiong, M.J. Lawson, D. Yuan, M. Hadjithomas, W. Miao, and E. Orias. 2013. Selecting one of several mating types through gene segment joining and deletion in Tetrahymena thermophila. *PLoS Biol.* 11:e1001518. https://doi.org/10.1371/journal.pbio.1001518

Cole, D.G., S.W. Chinn, K.P. Wedaman, K. Hall, T. Vuong, and J.M. Scholey. 1993. Novel heterotrimeric kinesin-related protein purified from sea urchin eggs. *Nature.* 366:268–270. https://doi.org/10.1038/366268a0

Couvillion, M.T., and K. Collins. 2012. Biochemical approaches including the design and use of strains expressing epitope-tagged proteins. *Methods Cell Biol.* 109:347–355. https://doi.org/10.1016/B978-0-12-385967-9.00012-8

Dafinger, C., M.C. Liebau, S.M. Elsayed, Y. Hellenbroich, E. Boltshauser, G.C. Korenke, F. Fabretti, A.R. Janecke, I. Ebermann, G. Nürnberg, et al. 2011. Mutations in KIF7 link Joubert syndrome with Sonic Hedgehog signaling and microtubule dynamics. *J. Clin. Invest.* 121:2662–2667. https://doi.org/10.1172/JCI43639

Das, A., D.J. Dickinson, C.C. Wood, B. Goldstein, and K.C. Slep. 2015. Crescerin uses a TOG domain array to regulate microtubules in the primary cilium. *Mol. Biol. Cell.* 26:4248–4264. https://doi.org/10.1091/mbc.e15-08-0603

Dave, D., D. Wloga, and J. Gaertig. 2009. Manipulating ciliary protein-encoding genes in Tetrahymena thermophila. *Methods Cell Biol.* 93:1–20. https://doi.org/10.1016/S0091-679X(08)93001-6

Dentler, W.L. 1980. Structures linking the tips of ciliary and flagellar microtubules to the membrane. *J. Cell Sci.* 42:207–220.

Dentler, W.L., and J.L. Rosenbaum. 1977. Flagellar elongation and shortening in Chlamydomonas. III. structures attached to the tips of flagellar microtubules and their relationship to the directionality of flagellar microtubule assembly. *J. Cell Biol.* 74:747–759. https://doi.org/10.1083/jcb.74.3.747

Duan, J., and M.A. Gorovsky. 2002. Both carboxy-terminal tails of alpha- and beta-tubulin are essential, but either one will suffice. *Curr. Biol.* 12:313–316. https://doi.org/10.1016/S0960-9822(02)00651-6

Evans, J.E., J.J. Snow, A.L. Gunnarson, G. Ou, H. Stahlberg, K.L. McDonald, and J.M. Scholey. 2006. Functional modulation of IFT kinesins extends the sensory repertoire of ciliated neurons in Caenorhabditis elegans. *J. Cell Biol.* 172:663–669. https://doi.org/10.1083/jcb.200509115

Fisch, C., and P. Dupuis-Williams. 2011. Ultrastructure of cilia and flagella - back to the future! *Biol. Cell.* 103:249–270. https://doi.org/10.1042/BC20100139

Fox, J.C., A.E. Howard, J.D. Currie, S.L. Rogers, and K.C. Slep. 2014. The XMAP215 family drives microtubule polymerization using a structurally diverse TOG array. *Mol. Biol. Cell.* 25:2375–2392. https://doi.org/10.1091/mbc.e13-08-0501

Funfak, A., C. Fisch, H.T. Abdel Motaal, J. Diener, L. Combettes, C.N. Baroud, and P. Dupuis-Williams. 2015. Paramecium swimming and ciliary beating patterns: a study on four RNA interference mutations. *Integr. Biol.* 7:90–100. https://doi.org/10.1039/C4IB00181H

Gaertig, J., D. Wloga, K.K. Vasudevan, M. Guha, and W. Dentler. 2013. Discovery and functional evaluation of ciliary proteins in Tetrahymena thermophila. *Methods Enzymol.* 525:265–284. https://doi.org/10.1016/B978-0-12-397944-5.00013-4

Gorovsky, M.A. 1973. Macro- and micronuclei of Tetrahymena pyriformis: a model system for studying the structure and function of eukaryotic nuclei. *J. Protozool.* 20:19–25. https://doi.org/10.1111/j.1550-7408.1973.tb05995.x

Goujon, M., H. McWilliam, W. Li, F. Valentin, S. Squizzato, J. Paern, and R. Lopez. 2010. A new bioinformatics analysis tools framework at EMBL-EBI. *Nucleic Acids Res.* 38(Web Server):W695–W699. https://doi.org/10.1093/nar/gkq313

Hai, B., J. Gaertig, and M.A. Gorovsky. 1999. Knockout heterokaryons enable facile mutagenic analysis of essential genes in Tetrahymena. *Methods Cell Biol.* 62:513–531. https://doi.org/10.1016/S0091-679X(08)61554-X

Hao, L., M. Thein, I. Brust-Mascher, G. Civelekoglu-Scholey, Y. Lu, S. Acar, B. Prevo, S. Shaham, and J.M. Scholey. 2011. Intraflagellar transport delivers tubulin isotypes to sensory cilium middle and distal segments. *Nat. Cell Biol.* 13:790–798. https://doi.org/10.1038/ncb2268

Haycraft, C.J., B. Banizs, Y. Aydin-Son, Q. Zhang, E.J. Michaud, and B.K. Yoder. 2005. Gli2 and Gli3 localize to cilia and require the intraflagellar transport protein polaris for processing and function. *PLoS Genet.* 1:e53. https://doi.org/10.1371/journal.pgen.0010053

He, M., R. Subramanian, F. Bangs, T. Omelchenko, K.F. Liem Jr., T.M. Kapoor, and K.V. Anderson. 2014. The kinesin-4 protein Kif7 regulates mammalian Hedgehog signalling by organizing the cilium tip compartment. *Nat. Cell Biol.* 16:663–672. https://doi.org/10.1038/ncb2988

Ichikawa, M., D. Liu, P.L. Kastritis, K. Basu, T.C. Hsu, S. Yang, and K.H. Bui. 2017. Subnanometre-resolution structure of the doublet microtubule reveals new classes of microtubule-associated proteins. *Nat. Commun.* 8:15035. https://doi.org/10.1038/ncomms15035

Insinna, C., N. Pathak, B. Perkins, I. Drummond, and J.C. Besharse. 2008. The homodimeric kinesin, Kif17, is essential for vertebrate photoreceptor sensory outer segment development. *Dev. Biol.* 316:160–170. https://doi.org/10.1016/j.ydbio.2008.01.025

Jaulin, F., and G. Kreitzer. 2010. KIF17 stabilizes microtubules and contributes to epithelial morphogenesis by acting at MT plus ends with EB1 and APC. *J. Cell Biol.* 190:443–460. https://doi.org/10.1083/jcb.201006044

Jerka-Dziadosz, M., I. Strzyewska-Jówko, U. Wojsa-Lugowska, W. Krawczyńska, and A. Krzywicka. 2001. The dynamics of filamentous structures in the apical band, oral crescent, fission line and the postoral meridional filament in Tetrahymena thermophila revealed by monoclonal antibody 12G9. *Protist.* 152:53–67. https://doi.org/10.1078/1434-4610-00043

Jiang, K., G. Toedt, S. Montenegro Gouveia, N.E. Davey, S. Hua, B. van der Vaart, I. Grigoriev, J. Larsen, L.B. Pedersen, K. Bezstarosti, et al. 2012. A Proteome-wide screen for mammalian SxIP motif-containing microtubule plus-end tracking proteins. *Curr. Biol.* 22:1800–1807. https://doi.org/10.1016/j.cub.2012.07.047

Jiang, L., B.M. Tam, G. Ying, S. Wu, W.W. Hauswirth, J.M. Frederick, O.L. Moritz, and W. Baehr. 2015a. Kinesin family 17 (osmotic avoidance abnormal-3) is dispensable for photoreceptor morphology and function. *FASEB J.* 29:4866–4880. https://doi.org/10.1096/fj.15-275677

Jiang, Y.Y., K. Lechtreck, and J. Gaertig. 2015b. Total internal reflection fluorescence microscopy of intraflagellar transport in Tetrahymena thermophila. *Methods Cell Biol.* 127:445–456. https://doi.org/10.1016/bs.mcb.2015.01.001

Kar, A., S.R. Phadke, A. Das Bhowmik, and A. Dalal. 2018. Whole exome sequencing reveals a mutation in ARMC9 as a cause of mental retardation, ptosis, and polydactyly. *Am. J. Med. Genet. A.* 176:34–40. https://doi.org/10.1002/ajmg.a.38537

Kubo, T., H.A. Yanagisawa, T. Yagi, M. Hirono, and R. Kamiya. 2010. Tubulin polyglutamylation regulates axonemal motility by modulating activities

of inner-arm dyneins. *Curr. Biol.* 20:441–445. https://doi.org/10.1016/j.cub.2009.12.058

Larkin, M.A., G. Blackshields, N.P. Brown, R. Chenna, P.A. McGettigan, H. McWilliam, F. Valentin, I.M. Wallace, A. Wilm, R. Lopez, et al. 2007. Clustal W and Clustal X version 2.0. *Bioinformatics.* 23:2947–2948. https://doi.org/10.1093/bioinformatics/btm404

Lechtreck, K.F., and S. Geimer. 2000. Distribution of polyglutamylated tubulin in the flagellar apparatus of green flagellates. *Cell Motil. Cytoskeleton.* 47:219–235. https://doi.org/10.1002/1097-0169(200011)47:3%3C219::AID-CM5%3E3.0.CO;2-Q

Lewis, T.R., S.R. Kundinger, A.L. Pavlovich, J.R. Bostrom, B.A. Link, and J.C. Besharse. 2017. Cos2/Kif7 and Osm-3/Kif17 regulate onset of outer segment development in zebrafish photoreceptors through distinct mechanisms. *Dev. Biol.* 425:176–190. https://doi.org/10.1016/j.ydbio.2017.03.019

Liem, K.F. Jr., M. He, P.J. Ocbina, and K.V. Anderson. 2009. Mouse Kif7/Costal2 is a cilia-associated protein that regulates Sonic hedgehog signaling. *Proc. Natl. Acad. Sci. USA.* 106:13377–13382. https://doi.org/10.1073/pnas.0906944106

Love, B., and M.B. Rotheim. 1984. Cell surface interactions in conjugation: Tetrahymena ciliary membrane vesicles. *Mol. Cell. Biol.* 4:681–687. https://doi.org/10.1128/MCB.4.4.681

McEwen, D.P., P.M. Jenkins, and J.R. Martens. 2008. Olfactory cilia: our direct neuronal connection to the external world. *Curr. Top. Dev. Biol.* 85:333–370. https://doi.org/10.1016/S0070-2153(08)00812-0

Mesland, D.A., J.L. Hoffman, E. Caligor, and U.W. Goodenough. 1980. Flagellar tip activation stimulated by membrane adhesions in Chlamydomonas gametes. *J. Cell Biol.* 84:599–617. https://doi.org/10.1083/jcb.84.3.599

Mitchell, D.R. 2003. Orientation of the central pair complex during flagellar bend formation in Chlamydomonas. *Cell Motil. Cytoskeleton.* 56:120–129. https://doi.org/10.1002/cm.10142

Mochizuki, K. 2008. High efficiency transformation of Tetrahymena using a codon-optimized neomycin resistance gene. *Gene.* 425:79–83. https://doi.org/10.1016/j.gene.2008.08.007

Moran, D.T., J.C. Rowley III, B.W. Jafek, and M.A. Lovell. 1982. The fine structure of the olfactory mucosa in man. *J. Neurocytol.* 11:721–746. https://doi.org/10.1007/BF01153516

Mukhopadhyay, S., Y. Lu, H. Qin, A. Lanjuin, S. Shaham, and P. Sengupta. 2007. Distinct IFT mechanisms contribute to the generation of ciliary structural diversity in C. elegans. *EMBO J.* 26:2966–2980. https://doi.org/10.1038/sj.emboj.7601717

Nelsen, E.M. 1978. Transformation in Tetrahymena thermophila. Development of an inducible phenotype. *Dev. Biol.* 66:17–31. https://doi.org/10.1016/0012-1606(78)90270-1

Nelsen, E.M., and L.E. Debault. 1978. Transformation in Tetrahymena pyriformis: description of an inducible phenotype. *J. Protozool.* 25:113–119. https://doi.org/10.1111/j.1550-7408.1978.tb03880.x

Omoto, C.K., and C. Kung. 1979. The pair of central tubules rotates during ciliary beat in Paramecium. *Nature.* 279:532–534. https://doi.org/10.1038/279532a0

Omoto, C.K., and C. Kung. 1980. Rotation and twist of the central-pair microtubules in the cilia of Paramecium. *J. Cell Biol.* 87:33–46. https://doi.org/10.1083/jcb.87.1.33

Omoto, C.K., I.R. Gibbons, R. Kamiya, C. Shingyoji, K. Takahashi, and G.B. Witman. 1999. Rotation of the central pair microtubules in eukaryotic flagella. *Mol. Biol. Cell.* 10:1–4. https://doi.org/10.1091/mbc.10.1.1

Orias, E., and L. Rasmussen. 1976. Dual capacity for nutrient uptake in Tetrahymena. IV. Growth without food vacuoles and its implications. *Exp. Cell Res.* 102:127–137. https://doi.org/10.1016/0014-4827(76)90307-4

Ou, G., O.E. Blacque, J.J. Snow, M.R. Leroux, and J.M. Scholey. 2005. Functional coordination of intraflagellar transport motors. *Nature.* 436:583–587. https://doi.org/10.1038/nature03818

Perkins, L.A., E.M. Hedgecock, J.N. Thomson, and J.G. Culotti. 1986. Mutant sensory cilia in the nematode Caenorhabditis elegans. *Dev. Biol.* 117:456–487. https://doi.org/10.1016/0012-1606(86)90314-3

Pfaffl, M.W. 2001. A new mathematical model for relative quantification in real-time RT-PCR. *Nucleic Acids Res.* 29:e45. https://doi.org/10.1093/nar/29.9.e45

Prevo, B., P. Mangeol, F. Oswald, J.M. Scholey, and E.J. Peterman. 2015. Functional differentiation of cooperating kinesin-2 motors orchestrates cargo import and transport in C. elegans cilia. *Nat. Cell Biol.* 17:1536–1545. https://doi.org/10.1038/ncb3263

Reese, T.S. 1965. Olfactory Cilia in the Frog. *J. Cell Biol.* 25:209–230. https://doi.org/10.1083/jcb.25.2.209

Reynolds, M.J., T. Phetruen, R.L. Fisher, K. Chen, B.T. Pentecost, G. Gomez, P. Ounjai, and H. Sui. 2018. The Developmental Process of the Growing Motile Ciliary Tip Region. *Sci. Rep.* 8:7977. https://doi.org/10.1038/s41598-018-26111-2

Rezabkova, L., S.H. Kraatz, A. Akhmanova, M.O. Steinmetz, and R.A. Kammerer. 2016. Biophysical and Structural Characterization of the Centriolar Protein Cep104 Interaction Network. *J. Biol. Chem.* 291:18496–18504. https://doi.org/10.1074/jbc.M116.739771

Roof, D., M. Adamian, D. Jacobs, and A. Hayes. 1991. Cytoskeletal specializations at the rod photoreceptor distal tip. *J. Comp. Neurol.* 305:289–303. https://doi.org/10.1002/cne.903050210

Roux, K.J., D.I. Kim, M. Raida, and B. Burke. 2012. A promiscuous biotin ligase fusion protein identifies proximal and interacting proteins in mammalian cells. *J. Cell Biol.* 196:801–810. https://doi.org/10.1083/jcb.201112098

Sale, W.S., and P. Satir. 1976. Splayed Tetrahymena cilia. A system for analyzing sliding and axonemal spoke arrangements. *J. Cell Biol.* 71:589–605. https://doi.org/10.1083/jcb.71.2.589

Sale, W.S., and P. Satir. 1977. The termination of the central microtubules from the cilia of Tetrahymena pyriformis. *Cell Biol. Int. Rep.* 1:45–49.

Salisbury, J.L., A.T. Baron, and M.A. Sanders. 1988. The centrin-based cytoskeleton of Chlamydomonas reinhardtii: distribution in interphase and mitotic cells. *J. Cell Biol.* 107:635–641. https://doi.org/10.1083/jcb.107.2.635

Sanders, A.A., E. de Vrieze, A.M. Alazami, F. Alzahrani, E.B. Malarkey, N. Sorusch, L. Tebbe, S. Kuhns, T.J. van Dam, A. Alhashem, et al. 2015. KIAA0556 is a novel ciliary basal body component mutated in Joubert syndrome. *Genome Biol.* 16:293. https://doi.org/10.1186/s13059-015-0858-z

Satir, P. 1968. Studies on cilia. 3. Further studies on the cilium tip and a "sliding filament" model of ciliary motility. *J. Cell Biol.* 39:77–94. https://doi.org/10.1083/jcb.39.1.77

Satish Tammana, T.V., D. Tammana, D.R. Diener, and J. Rosenbaum. 2013. Centrosomal protein CEP104 (Chlamydomonas FAP256) moves to the ciliary tip during ciliary assembly. *J. Cell Sci.* 126:5018–5029. https://doi.org/10.1242/jcs.133439

Schiapparelli, L.M., D.B. McClatchy, H.H. Liu, P. Sharma, J.R. Yates III, and H.T. Cline. 2014. Direct detection of biotinylated proteins by mass spectrometry. *J. Proteome Res.* 13:3966–3978. https://doi.org/10.1021/pr5002862

Schneider, C.A., W.S. Rasband, and K.W. Eliceiri. 2012. NIH Image to ImageJ: 25 years of image analysis. *Nat. Methods.* 9:671–675. https://doi.org/10.1038/nmeth.2089

Schwarz, N., A. Lane, K. Jovanovic, D.A. Parfitt, M. Aguila, C.L. Thompson, L. da Cruz, P.J. Coffey, J.P. Chapple, A.J. Hardcastle, and M.E. Cheetham. 2017. Arl3 and RP2 regulate the trafficking of ciliary tip kinesins. *Hum. Mol. Genet.* 26:2480–2492. https://doi.org/10.1093/hmg/ddx143

Shaheen, R., K. Szymanska, B. Basu, N. Patel, N. Ewida, E. Faqeih, A. Al Hashem, N. Derar, H. Alsharif, M.A. Aldahmesh, et al. Ciliopathy Working Group. 2016. Characterizing the morbid genome of ciliopathies. *Genome Biol.* 17:242. https://doi.org/10.1186/s13059-016-1099-5

Shaner, N.C., G.G. Lambert, A. Chammas, Y. Ni, P.J. Cranfill, M.A. Baird, B.R. Sell, J.R. Allen, R.N. Day, M. Israelsson, et al. 2013. A bright monomeric green fluorescent protein derived from Branchiostoma lanceolatum. *Nat. Methods.* 10:407–409. https://doi.org/10.1038/nmeth.2413

Shang, Y., B. Li, and M.A. Gorovsky. 2002. Tetrahymena thermophila contains a conventional gamma-tubulin that is differentially required for the maintenance of different microtubule-organizing centers. *J. Cell Biol.* 158:1195–1206. https://doi.org/10.1083/jcb.200205101

Signor, D., K.P. Wedaman, L.S. Rose, and J.M. Scholey. 1999. Two heteromeric kinesin complexes in chemosensory neurons and sensory cilia of Caenorhabditis elegans. *Mol. Biol. Cell.* 10:345–360. https://doi.org/10.1091/mbc.10.2.345

Snow, J.J., G. Ou, A.L. Gunnarson, M.R. Walker, H.M. Zhou, I. Brust-Mascher, and J.M. Scholey. 2004. Two anterograde intraflagellar transport motors cooperate to build sensory cilia on C. elegans neurons. *Nat. Cell Biol.* 6:1109–1113. https://doi.org/10.1038/ncb1186

Srour, M., F.F. Hamdan, D. McKnight, E. Davis, H. Mandel, J. Schwartzentruber, B. Martin, L. Patry, C. Nassif, A. Dionne-Laporte, et al. Care4Rare Canada Consortium. 2015. Joubert Syndrome in French Canadians and Identification of Mutations in CEP104. *Am. J. Hum. Genet.* 97:744–753. https://doi.org/10.1016/j.ajhg.2015.09.009

Stepanek, L., and G. Pigino. 2016. Microtubule doublets are double-track railways for intraflagellar transport trains. *Science.* 352:721–724. https://doi.org/10.1126/science.aaf4594

Suprenant, K.A., and W.L. Dentler. 1988. Release of intact microtubule-capping structures from Tetrahymena cilia. *J. Cell Biol.* 107:2259–2269. https://doi.org/10.1083/jcb.107.6.2259

Suryavanshi, S., B. Eddé, L.A. Fox, S. Guerrero, R. Hard, T. Hennessey, A. Kabi, D. Malison, D. Pennock, W.S. Sale, et al. 2010. Tubulin glutamylation regulates ciliary motility by altering inner dynein arm activity. *Curr. Biol.* 20:435–440. https://doi.org/10.1016/j.cub.2009.12.062

Tsypin, L.M., and A.P. Turkewitz. 2017. The Co-regulation Data Harvester: automating gene annotation starting from a transcriptome database. *SoftwareX.* 6:165–171. https://doi.org/10.1016/j.softx.2017.06.006

Tukachinsky, H., L.V. Lopez, and A. Salic. 2010. A mechanism for vertebrate Hedgehog signaling: recruitment to cilia and dissociation of SuFu-Gli protein complexes. *J. Cell Biol.* 191:415–428. https://doi.org/10.1083/jcb.201004108

Urbanska, P., K. Song, E. Joachimiak, L. Krzemien-Ojak, P. Koprowski, T. Hennessey, M. Jerka-Dziadosz, H. Fabczak, J. Gaertig, D. Nicastro, and D. Wloga. 2015. The CSC proteins FAP61 and FAP251 build the basal substructures of radial spoke 3 in cilia. *Mol. Biol. Cell.* 26:1463–1475. https://doi.org/10.1091/mbc.e14-11-1545

Van De Weghe, J.C., T.D.S. Rusterholz, B. Latour, M.E. Grout, K.A. Aldinger, R. Shaheen, J.C. Dempsey, S. Maddirevula, Y.H. Cheng, I.G. Phelps, et al. University of Washington Center for Mendelian Genomics. 2017. Mutations in ARMC9, which Encodes a Basal Body Protein, Cause Joubert Syndrome in Humans and Ciliopathy Phenotypes in Zebrafish. *Am. J. Hum. Genet.* 101:23–36. https://doi.org/10.1016/j.ajhg.2017.05.010

Westermann, S., A. Avila-Sakar, H.W. Wang, H. Niederstrasser, J. Wong, D.G. Drubin, E. Nogales, and G. Barnes. 2005. Formation of a dynamic kinetochore- microtubule interface through assembly of the Dam1 ring complex. *Mol. Cell.* 17:277–290. https://doi.org/10.1016/j.molcel.2004.12.019

Widlund, P.O., J.H. Stear, A. Pozniakovsky, M. Zanic, S. Reber, G.J. Brouhard, A.A. Hyman, and J. Howard. 2011. XMAP215 polymerase activity is built by combining multiple tubulin-binding TOG domains and a basic lattice-binding region. *Proc. Natl. Acad. Sci. USA.* 108:2741–2746. https://doi.org/10.1073/pnas.1016498108

Wloga, D., A. Camba, K. Rogowski, G. Manning, M. Jerka-Dziadosz, and J. Gaertig. 2006. Members of the NIMA-related kinase family promote disassembly of cilia by multiple mechanisms. *Mol. Biol. Cell.* 17:2799–2810. https://doi.org/10.1091/mbc.e05-05-0450

Wolfe, J., R. Turner Jr., R. Barker, and W.S. Adair. 1979. The need for an extracellular component for cell pairing in Tetrahymena. *Exp. Cell Res.* 121:27–30. https://doi.org/10.1016/0014-4827(79)90440-3

Xiong, J., Y. Lu, J. Feng, D. Yuan, M. Tian, Y. Chang, C. Fu, G. Wang, H. Zeng, and W. Miao. 2013. Tetrahymena functional genomics database (TetraFGD): an integrated resource for Tetrahymena functional genomics. *Database (Oxford).* 2013:bat008. https://doi.org/10.1093/database/bat008

Ye, F., A.R. Nager, and M.V. Nachury. 2018. BBSome trains remove activated GPCRs from cilia by enabling passage through the transition zone. *J. Cell Biol.* 217:1847–1868. https://doi.org/10.1083/jcb.201709041

Supplemental material

Louka et al., https://doi.org/10.1083/jcb.201804141

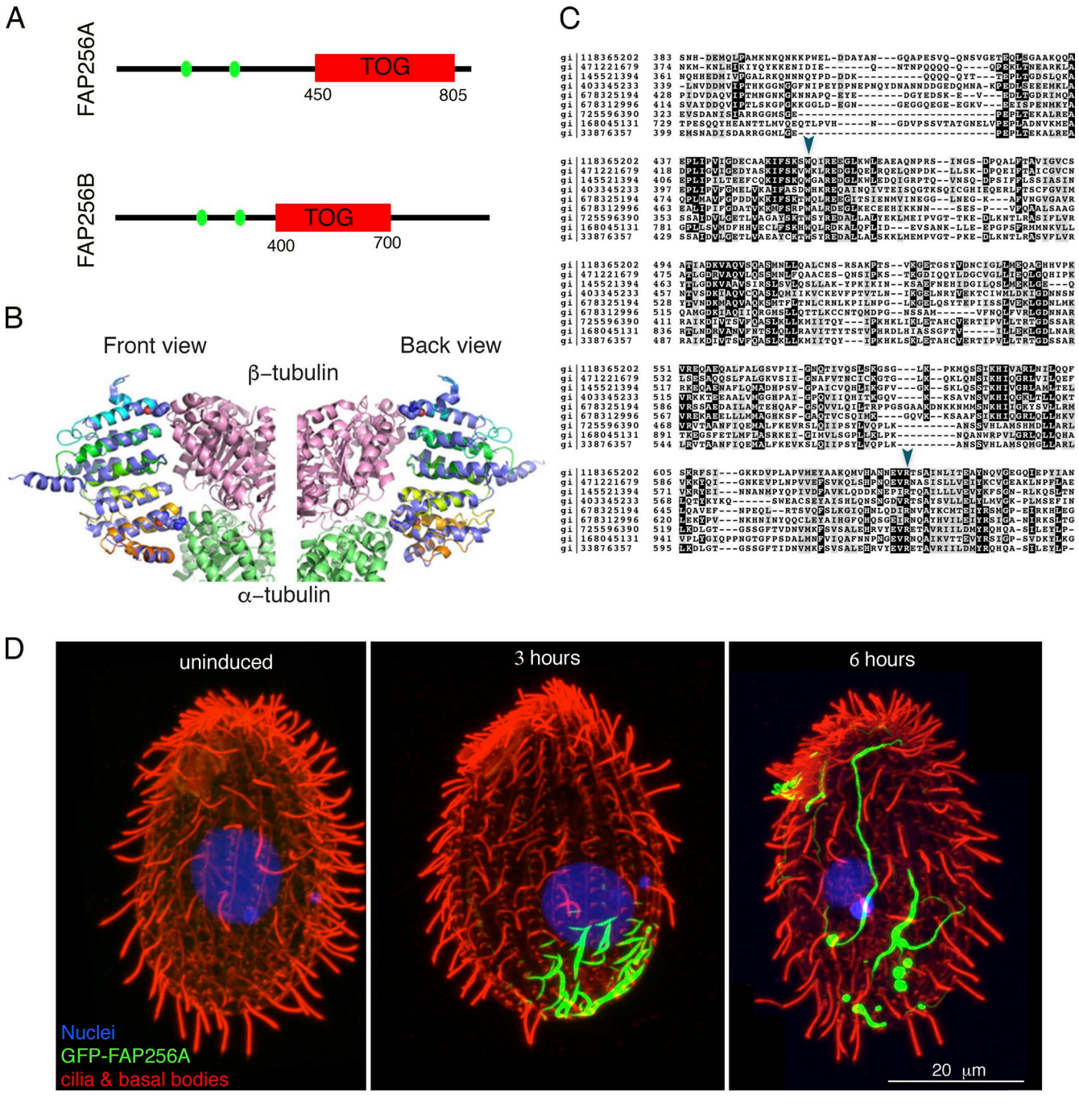

Figure S1. ***Tetrahymena* FAP256 is a TOG-domain protein that oligomerizes. (A)** Domain organization of FAP256/CEP104 *Tetrahymena* homologues based on the InterPro database (red box, TOG domain, amino acids 450–805 in FAP256A and amino acids 400–700 in FAP256B; green circle, coiled-coil domain). **(B)** A 3D model of the TOG domain of FAP256A predicted using i-TASSER (rainbow colors), superimposed on the crystal structure of Stu2:TOG1-αβ-tubulin (slate, Stu2:TOG1; pink, β-tubulin; green, α-tubulin). **(C)** A multiple sequence alignment of CEP104/FAP256 homologues. The sequences used were from *Tetrahymena thermophila* gi|118365202 (FAP256A), *Ichthyophthirius multifiliis* gi|471221679, *Paramecium tetraurelia* gi|145521394, *Oxytricha trifallax* gi|403345233, *Stylonychia lemnae* gi|678325194 and gi|678312996, *Saimiri boliviensis* gi|725596390, *Physcomitrella patens* gi|168045131, and *Homo sapiens* gi|33876357 (the arrowheads mark the conserved amino acids that form the interphase with curved tubulin). **(D)** Confocal immunofluorescence images of *Tetrahymena* cells expressing GFP-FAP256A under the control of the cadmium inducible promoter *MTT1*. Cells were fixed before transgene induction and 3 and 6 h after induction with 2.5 μg/ml $CdCl_2$ (green, GFP-FAP256A; blue, DAPI; red, α-tubulin, polyG, and centrin).

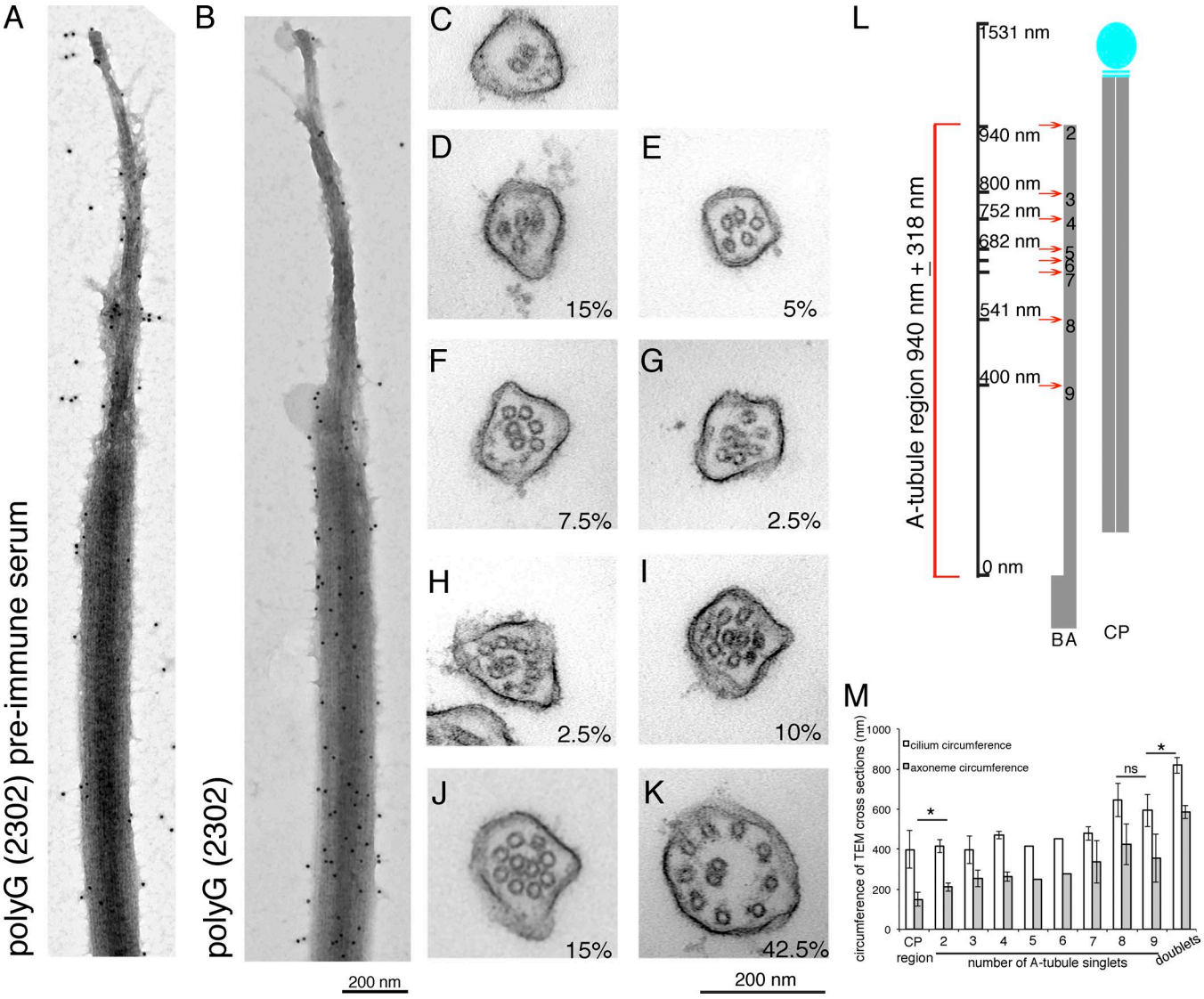

Figure S2. **The distal segment is defined by the termination of B-tubules, absence of polyG, and a decrease in the cilium and axoneme diameter. (A and B)** Immunoelectron microscopy localization of polyglycylated tubulin (using polyG antibodies) in cilia. Representative immunoelectron micrographs of isolated axonemes labeled with either the preimmune serum (A) or antibodies against polyglycylated tubulin (polyG 2302; B) and gold-conjugated secondary antibodies. **(C–K)** Representative TEM cross sections of wild-type cilia within the distal segment. A cross section through the CP region (C). Cross sections through the A-tubule region (D–K). The percentages of cross sections with different numbers of A-tubules (bottom right corner) were calculated in the total of 40 cross sections. The number of cross sections with two A-tubules: 6 (D); three A-tubules: 2 (E); four A-tubules: 3 (F); five A-tubules: 1 (G); six A-tubules: 1 (H); seven A-tubules: 4 (I); eight A-tubules: 6 (J); and nine A-tubules: 17 (K). **(L)** A cartoon showing the estimated positions of termination points of A-tubules within the distal segment. The numbers on the A-tubule show the number of singlets at the position marked by the red arrow. We did not find cross sections with one A-tubule. The position of each A-tubule termination is presented as the distance (in nanometers) from the B-tubule termination zone. **(M)** Quantification of cilium and axoneme circumference using TEM cross sections through the middle and distal segment. Error bars show standard deviation and asterisk marks statistical significance (two-sided *t* test, $P < 0.05$; ns, not significant).

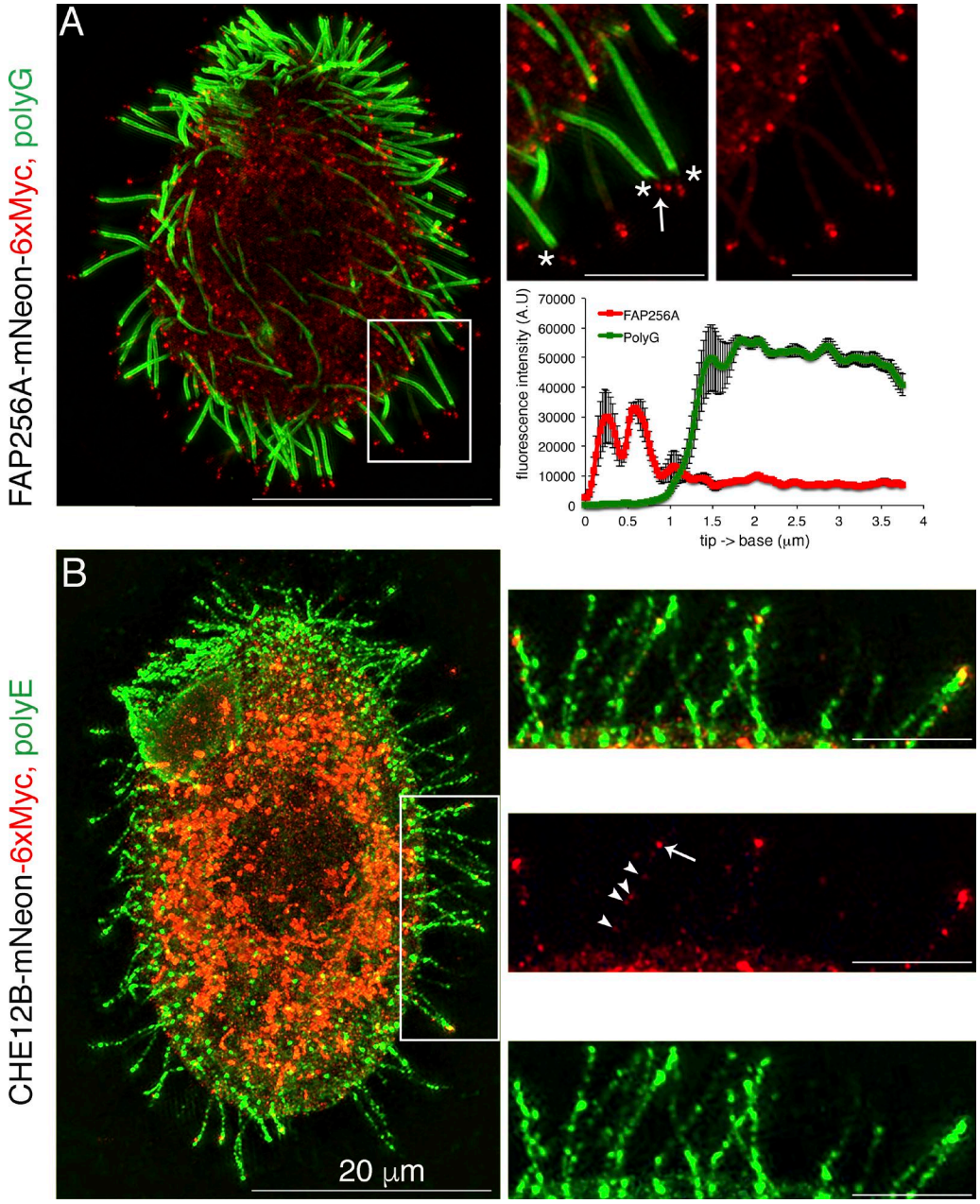

Figure S3. **FAP256A and CHE12B localize to different compartments near the ends of cilia. (A and B)** SR-SIM immunofluorescence images of *Tetrahymena* cells expressing either FAP256A-2xmNeonGreen-6xMyc-BirA (A) or CHE12B-mNeon-6xMyc-BirA* (B) under native promoter. Cilia were labeled with polyG (A; green) or polyE (B; green), and FAP256A and CHE12B were detected using an anti-Myc antibody (red). In A (magnified image) the asterisk marks the gap between the FAP256A and polyG tubulin signal, the average fluorescence intensity of these cilia was plotted over the cilium length (error bars show standard deviation, n = 3 cilia). In B (magnified image) the arrow and arrowheads mark the CHE12B signals near the tip and along the cilium, respectively (bars: 20 μm [main], 5 μm [inset]).

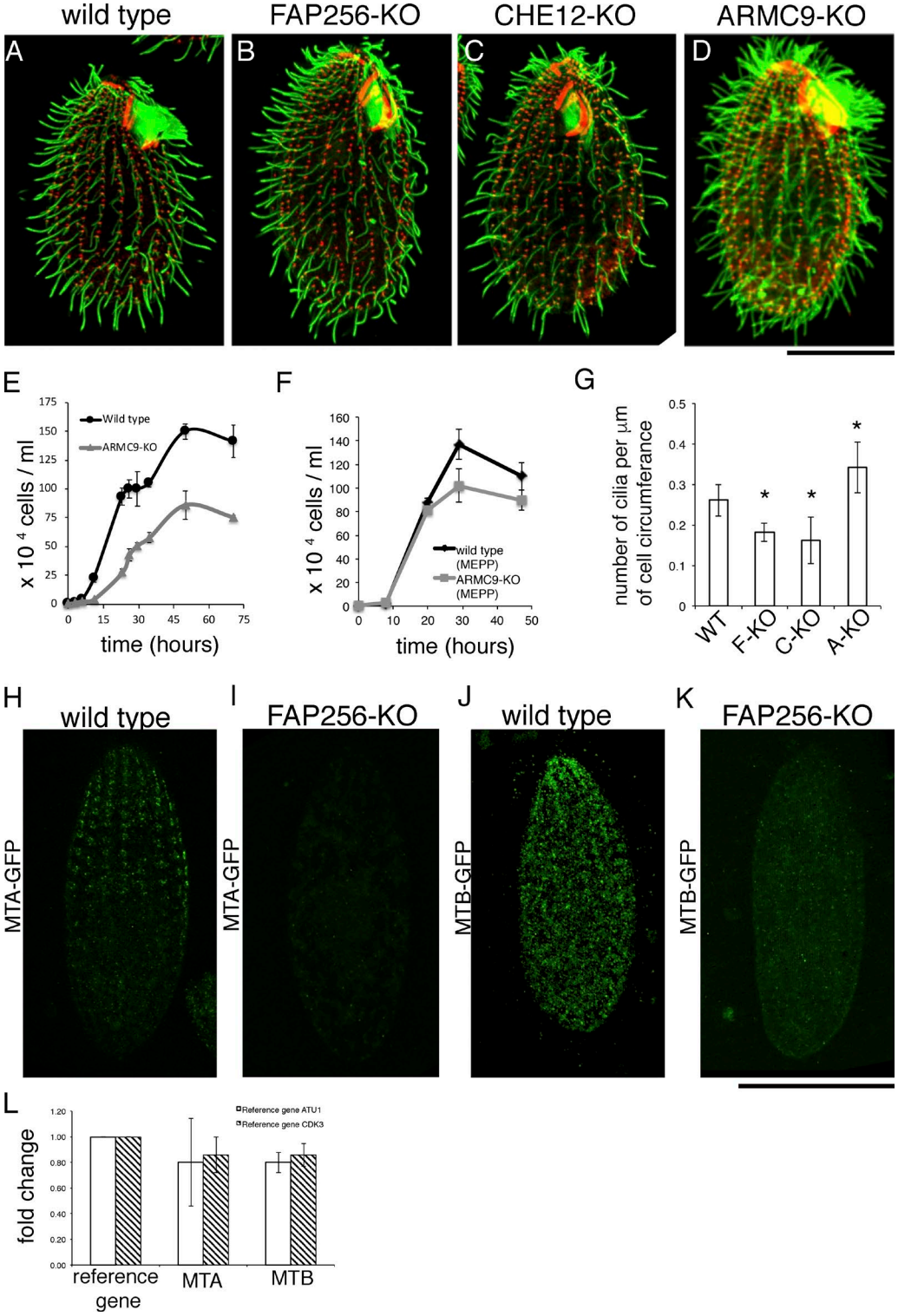

Figure S4. **The morphology, growth rates, and ciliation of the wild-type and KO strains. (A–D)** Confocal immunofluorescence images of wild-type, FAP256-KO, CHE12-KO, and ARMC9-KO cells stained with polyG antibodies (green) and anti-centrin (red). Growth curves of wild-type and ARMC9 KO cultures in SPP (E) and MEPP media (F). **(G)** Cilia densities (number of cilia per micrometer of cell circumference) were calculated by dividing the number of visible cilia at the widest cell circumference by the length of the circumference (WT: 0.27 cilia/µm, ±0.05 *n* = 10; F-KO: 0.18 cilia/µm, ±0.02 *n* = 8; C-KO: 0.18 cilia/µm, ±0.05 *n* = 12; and A-KO: 0.34 cilia/µm, ±0.06 *n* = 10; asterisks show significant differences compared with wild type; two-sided *t* test, $P < 0.05$). **(H–K)** SR-SIM images of wild type (H and J) and FAP256AB-KO cells (I and K) expressing either MTA4-GFP (H and I) or MTB4-GFP (J and K) based on engineering the native loci. **(L)** Quantification of mRNA levels of MTA (TTHERM_01087800) and MTB (TTHERM_01087820) in FAP256-KO–starvedcells; data were normalized using two different reference genes (ATU1 [TTHERM_00558620] or CDK3 [TTHERM_00339880]). The fold change in the knockout over the wild type is shown. Error bars show standard deviation (*n* = 2 independent RNA and cDNA preparations, all samples were analyzed on the same plate, two-sided *t* test; no difference; bars, 20 µm).

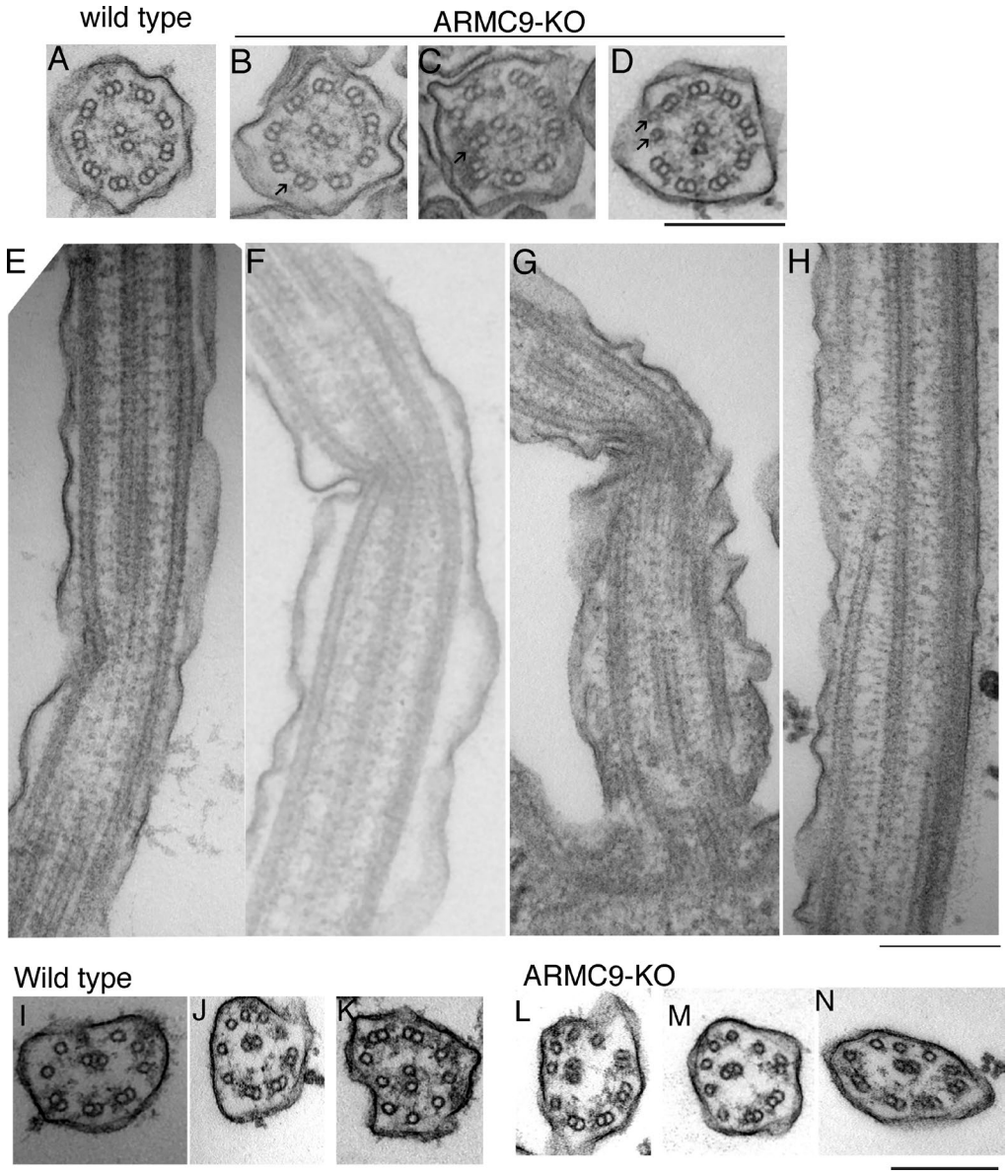

Figure S5. **A loss of ARMC9 causes infrequent structural defects in the middle segment. (A–H)** Representative cross section of a wild-type cilium (A) and ARMC9-KO cilia showing missing outer dynein arms (B), a doublet that is 90° rotated in relation to the CP (C) and a split doublet (D). Longitudinal sections showing areas of extensive bend (E–G) and collapsed outer doublets (H) in the ARMC9-KO cilia. **(I–N)** In both the wild type (I–K) and ARMC9-KO (L–N) cilia, the transition of the outer microtubule from a doublet to a singlet conformation correlates with termination of radial spokes and displacement of the outer microtubule and its adjacent portion of the membrane closer to the cilium center. The images represent cross sections of cilia containing both singlet and doublet microtubules and therefore corresponding to the transitional region between the middle and distal segment (bars, 200 nm).

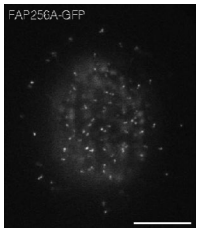

Video 1. **A TIRFM video of a cell expressing FAP256A-GFP.** Notice the two adjacent FAP256 foci move together. Video played at 7 fps. Bar, 20 µm.

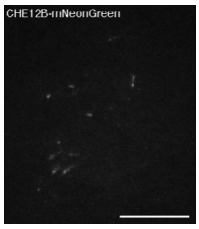

Video 2. **A TIRFM video of a cell expressing CHE12B-mNeonGreen.** Video played at 7 fps. Bar, 20 µm.

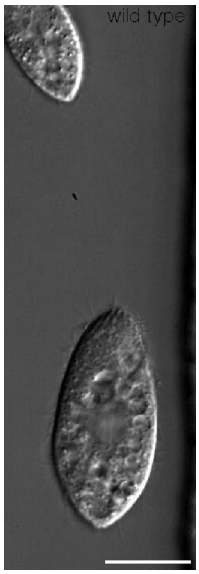

Video 3. **High speed video of a wild-type cell freely swimming in a microfluidic channel.** The video was recorded at 2,000 fps and played at 10 fps. Bar, 20 µm.

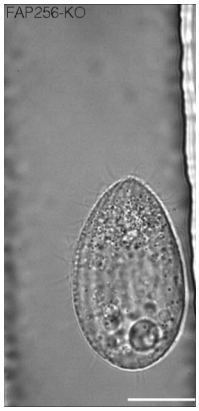

Video 4. **High speed video of a FAP256-KO cell freely swimming in a microfluidic channel.** The video was recorded at 2,000 fps and played at 10 fps. Bar, 20 µm.

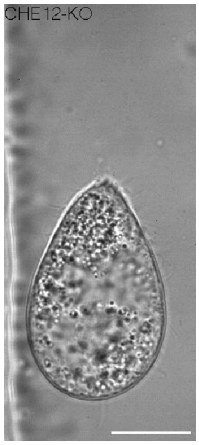

Video 5. **High speed video of a CHE12-KO cell freely swimming in a microfluidic channel.** The video was recorded at 2,000 fps and played at 10 fps. Bar, 20 µm.

Video 6. **High speed video of an ARMC9-KO cell freely swimming in a microfluidic channel.** The video was recorded at 2,000 fps and played at 10 fps. Bar, 20 µm.

Tables S1–S4 are provided as separate Excel files. Table S1 includes all primers used for amplification of coding sequences for tagging of the native loci, overexpression, gene disruptions, and genotyping. Table S2 shows the distal segment-associated protein candidates with at least 10-fold enrichment in BirA*-NRK2-(K35R)-GFP as compared with GFP-BirA*-expressing cilia. Table S3 lists the primers used for quantification of gene expression by qRT-PCR. Table S4 summarizes all the defects caused by the loss of either FAP256 or CHE12 or ARMC9 in Tetrahymena.